Validating a minipig model of reversible cerebral demyelination using human diagnostic modalities and electron microscopy

Mihai Ancău,[a,b,o,p] Goutam Kumar Tanti,[a,p] Vicki Marie Butenschoen,[c] Jens Gempt,[c,d] Igor Yakushev,[e] Stephan Nekolla,[e] Mark Mühlau,[a] Christian Scheunemann,[f,g] Sebastian Heininger,[f,g] Benjamin Löwe,[f,g] Erik Löwe,[f,g] Silke Baer,[h] Johannes Fischer,[h] Judith Reiser,[h] Sai S. Ayachit,[a,i] Friederike Liesche-Starnecker,[j,k] Jürgen Schlegel,[j] Kaspar Matiasek,[l] Martina Schifferer,[b,m] Jan S. Kirschke,[n] Thomas Misgeld,[b,m,o] Tim Lueth,[f,g] and Bernhard Hemmer[a,b,*]

[a]Department of Neurology, Klinikum Rechts der Isar, School of Medicine and Health, Technical University of Munich, Munich, Germany
[b]Munich Cluster for Systems Neurology (SyNergy), Munich, Germany
[c]Department of Neurosurgery, Klinikum Rechts der Isar, School of Medicine and Health, Technical University of Munich, Germany
[d]Department of Neurosurgery, University Medical Center Hamburg-Eppendorf, Hamburg, Germany
[e]Department of Nuclear Medicine, Klinikum Rechts der Isar, School of Medicine and Health, Technical University of Munich, Germany
[f]Institute of Micro Technology and Medical Device Technology, Technical University of Munich, Garching, Germany
[g]Ergosurg GmbH, Ismaning, Germany
[h]Centre for Preclinical Research, Department of Veterinary Medicine, Technical University of Munich, Munich, Germany
[i]Graduate School of Systemic Neurosciences, Ludwig Maximilian University of Munich, Germany
[j]Department of Neuropathology, Institute of Pathology, Technical University of Munich School of Medicine, Munich, Germany
[k]Medical Faculty, Institute of Pathology and Molecular Diagnostics, University of Augsburg, Augsburg, Germany
[l]Clinical and Comparative Neuropathology, Centre for Clinical Veterinary Medicine, Ludwig-Maximilians-University, Munich, Germany
[m]German Center for Neurodegenerative Diseases (DZNE), Munich, Germany
[n]Department of Neuroradiology, Klinikum Rechts der Isar, School of Medicine and Health, Technical University of Munich, Germany
[o]Institute of Neuronal Cell Biology, School of Medicine and Health, Technical University of Munich, Munich, Germany

Summary

Background Inflammatory demyelinating diseases of the central nervous system, such as multiple sclerosis, are significant sources of morbidity in young adults despite therapeutic advances. Current murine models of remyelination have limited applicability due to the low white matter content of their brains, which restricts the spatial resolution of diagnostic imaging. Large animal models might be more suitable but pose significant technological, ethical and logistical challenges.

Methods We induced targeted cerebral demyelinating lesions by serially repeated injections of lysophosphatidylcholine in the minipig brain. Lesions were amenable to follow-up using the same clinical imaging modalities (3T magnetic resonance imaging, ^{11}C-PIB positron emission tomography) and standard histopathology protocols as for human diagnostics (myelin, glia and neuronal cell markers), as well as electron microscopy (EM), to compare against biopsy data from two patients.

Findings We demonstrate controlled, clinically unapparent, reversible and multimodally trackable brain white matter demyelination in a large animal model. De-/remyelination dynamics were slower than reported for rodent models and paralleled by a degree of secondary axonal pathology. Regression modelling of ultrastructural parameters (g-ratio, axon thickness) predicted EM features of cerebral de- and remyelination in human data.

Interpretation We validated our minipig model of demyelinating brain diseases by employing human diagnostic tools and comparing it with biopsy data from patients with cerebral demyelination.

*Corresponding author. Department of Neurology, Klinikum Rechts der Isar, School of Medicine and Health, Technical University of Munich, Munich, Germany.
E-mail address: hemmer@tum.de (B. Hemmer).
[p]These authors contributed equally: Mihai Ancău, Goutam Kumar Tanti.

Research in context

Evidence before this study

Inflammatory demyelinating diseases of the central nervous system (CNS), targeting the white matter (WM) of the brain and spinal cord, such as multiple sclerosis (MS), represent some of the most common non-traumatic causes of disability in young adults. Murine models, for example, experimental autoimmune encephalomyelitis, have been demonstrated to depict pathophysiological facets of human disease reliably. However, their low WM content limits validity, while their diminutive brain sizes limit the availability of neuroimaging tools of equal resolution to the diagnostic imaging tools used in a clinical context in human patients.

Added value of this study

Here, we established a model of demyelinating brain diseases in the minipig by developing a platform for Minipig Stereotactic White-matter Injection using Navigation by Electromagnetism (MiniSWINE). Specifically, to overcome the neuroanatomical challenges of stereotactic injection in the pig brain, we designed an electromagnetic-guided tracking system whose key advantage is the direct and in situ measurement of the position of the injection cannula tip.

Moreover, we validated the platform and characterised the minipig model using clinically relevant neuroimaging and microscopy tools and by comparison with EM data from biopsies obtained from patients with inflammatory demyelinating diseases. Notably, we performed this characterisation at different disease stages, reflecting successive stages of de- and remyelination. The remyelination dynamics inferred in this study exhibited incomplete remyelination at the latest such stage (subacute), with persistent astroglial and microglial activation and a minor degree of secondary axonal degeneration.

Implications of all the available evidence

The MiniSWINE model combines well-established demyelination-induction methods from rodent models of CNS demyelinating diseases and clinically relevant human neuroimaging tools. It provides a platform for the potential development of diagnostic procedures, the discovery of imaging biomarkers and the testing of remyelinating agents in diseases such as MS. Additionally, our electromagnetic-guided injection technique may enhance stereotactic substance delivery in human neurosurgery.

Introduction

Inflammatory demyelinating diseases of the central nervous system (CNS), including multiple sclerosis (MS), neuromyelitis optica (NMO), acute disseminated encephalomyelitis (ADEM) or MOG-antibody-associated disease (MOGAD), represent the most common non-traumatic causes of disability in young adults, afflicting more than 2.5 million people worldwide.[1] Magnetic resonance imaging (MRI) allows for assessing brain and spinal cord lesions in these diseases and thus has become an essential tool for clinical care. However, it still is not fully understood which MRI signatures relate to which histopathological stage of lesion evolution, such as the critical transition from demyelination to remyelination.[2] Refining the imaging readout for remyelination in early clinical trials is one of the main challenges limiting the development of remyelinating therapies for MS.[3] While rodent models of demyelinating CNS disorders would be logistically convenient to devise novel diagnostic MRI- and positron emission tomography (PET)-techniques, these models are not optimal for immediate translation because of the small size, relatively low white matter (WM) content and the lissencephalic nature of their brains, as well as due to genomic and proteomic discrepancies between rodents and humans.[4–6]

An animal model with larger brain size and neuro-anatomic features closer to humans would not have such limitations. Moreover, a model would be optimal if, throughout successive stages of lesions, de- and remyelination could be detected with the same diagnostic protocols and, ideally, devices as in human clinical settings. Here, we report such a model based on refined stereotactic microinjection of lysophosphatidylcholine (LPC) into the cerebral WM of minipigs. Minipigs are not a distinct pig species from the larger, landrace swine but a variety of breeds that have been selected to be reduced in size and constitute some of the smallest known domestic swine (*Sus scrofa domesticus*).[7] Pigs are increasingly used for biomedical research, for instance, in xenotransplantation or testing of human therapeutic antibodies.[8–10] Neurological diseases that have already been modelled in the minipig subspecies include Parkinson's disease, Huntington's disease and experimental autoimmune encephalomyelitis (EAE).[11–13]

Temporally and spatially controlled LPC microinjections induce sequential de- and remyelination at pre-determined locations in rodents.[5,14] Such control can

minimise neurological deficits and ethical constraints for CNS demyelinating disease modelling—including in pigs. Also, LPC and ethidium bromide-induced demyelination have been proven to lead to signs compatible with demyelination in the cerebral WM of large, domestic landrace pigs[15] and demonstrated demyelination in the rabbit cerebral WM[16] and the non-human primate (macaque) optic nerve.[17] However, there is considerable heterogeneity in the reported timelines of myelin-related events across species, ranging from reports of relatively quick demyelination (i.e., ensuing within 30 min and reaching full extent within four days[18] and complete remyelination without evidence of substantial axonal damage within 5–6 weeks in the case of rodent models),[19–21] to persistent demyelination conducive of axonal degeneration even eight weeks after LPC injection in the macaque optic nerve.[17] Interspecies differences such as the degree of collateral inflammation, the efficiency of lesion repopulation by oligodendrocyte progenitor cells (OPC), lesion volume, and reduction in oligodendroglial support to axons have all been postulated to contribute to the wide range of myelination and neurodegeneration responses.[17] Recently, a study of focal WM lesions in marmoset EAE showed sensitive and specific detection of remyelination using a 7T multisequence MRI. However, it used validation via immunohistochemistry (IHC) and not electron microscopy (EM), which could over/underestimate the extent of remyelination.[22] All-in-all, there is still unclarity as to the proportion in which canonical MRI sequences can reliably track de- and remyelination in large animal models of CNS pathology, pending validation, ideally via ultrastructural analysis, to assess whether they more accurately model human disease.

For systematic and reliable placement of demyelinating lesions in the CNS of minipigs, we used computer-assisted navigation (CAN) and convection-enhanced delivery (CED), allowing for sufficient LPC penetration regardless of injection depth inside the tissue. CAN technologies that rely on electromagnetic tracking systems[23] (EMTS) avoid imprecision due to instrument bending during surgery since they derive the position and orientation of the instrument by measuring currents induced by an electromagnetic field using sensors at the instrument's tip rather than by extrapolation from imaging the shaft, as in optical tracking systems (OTS). The essential advantage of the EMTS we designed, compared to current techniques used in human neurosurgery, is its full compatibility with bendable instruments because, in addition to precisely measuring the tip position, the shape of the bend can also be detected, and undesirable deformations rectified.

Using these neurosurgical innovations, we report here an EMTS platform for ***Mini**pig **S**tereotactic **W**hite-matter **I**njection using **N**avigation by **E**lectromagnetism* (*MiniSWINE*), which enables precise spatiotemporally

controlled induction of demyelinating lesions in the minipig brain. We characterise and validate the minipig brain model of demyelinating diseases via longitudinal follow-up using diagnostic MRI protocols from human neuroradiology, ^{11}C-PIB-PET, and neuro-histopathology, as well as by comparison with biopsies from patients with inflammatory demyelinating diseases by electron microscopy.

Methods
Ethics
The animal study complied with the EU Directive 2010/63/EU for animal experiments and the German Animal Welfare Act. The Ethics Committee for Animal Experiments of the Government of Upper Bavaria, Munich, Germany, approved all animal procedures (Reference number ROB 55.2-2532.Vet_02-18-82). Since we aimed at inducing clinically unapparent lesions, the emergence of neurological deficits in the animals represented a humane endpoint. Regarding patient biopsies, written informed consent was obtained from each participant treated in the Department of Neurology, Klinikum rechts der Isar, Technical University of Munich, Germany. Samples were collected as part of the department's biobank project, which pertains to the Joint Biobank Munich in the framework of the German Biobank Nodes.

Animals
A total of 9 young, healthy adult Aachen minipigs[24] (aged 19 ± 1 months at entry in the experiment, with a life expectancy of 15–20 years), weighing 60.2 ± 2.32 kg (3 males and 6 females) were used in this study. The animals were fed rationed feed rich in crude fibre. Water was provided ad libitum. We housed animals together, at least in pairs. Before the start of the study and daily after the beginning of the experiment, each animal was given a clinical examination by a veterinarian. The minipigs were acclimatised to the study procedures for at least two weeks.

From the total possible number of 108 lesions of a particular stage in our 9 animals, 28 lesions dropped out due to premature experiment termination when neurological deficits appeared. Furthermore, we excluded from the analysis lesions with a volume of intracerebral haemorrhage higher than 100 mm³, ending up with 60 lesions suitable for analysis (Supplementary Figure S1).

Human samples
Patient A (*acute, aHum*), a 19-year-old female, needed a diagnostic stereotactic biopsy from the clinically manifest cerebellar white matter lesion and was later diagnosed with relapsing-remitting MS. Patient S (*subacute, sHum*), a 68-year-old male, had a diagnostic stereotactic biopsy from the right parietal subcortical white matter

ascertaining the diagnosis of ADEM at a subacute stage. The tissue probe was taken after an initial positive response to *ex juvantibus* immunosuppressive therapy (1 g methylprednisolone intravenously per day over five days), providing time for incipient remyelination of the biopsied plaque.

Experimental timeline

At an interval of 10 ± 3 days before the first surgery, we performed an initial CT and Gd-enhanced MRI scan under general anaesthesia to aid subsequent surgeries and injection trajectory planning. Next, three pairs of stereotactic injections were performed in the cerebral WM. Each couple of injections was separated by 10 ± 3 days, targeting distinct bilateral symmetric localisations. On the same day as the 2nd pair of injections, within an hour from the end of the surgery, as well as 10 ± 3 days after the 3rd injection, we performed PET-MRI scans (Fig. 1a). The MRI scans primarily allowed for longitudinal follow-up of lesions over acute (10 days post-induction, dpi), intermediate (20 dpi) and subacute stages (30 dpi) and were performed according to standard sequence protocols recommended in the diagnosis of MS. The rationale for 10 ± 3 days between imaging sessions was grounded in data regarding de- and remyelination latencies from studies of large-animal demyelination models.[15–17] The variability of the interscan intervals was mainly conditioned by scanner availability due to parallel use for humans in a clinical setting. The longitudinal PET scans were performed in the acute and subacute stages using ^{11}C-labeled Pittsburgh compound B (^{11}C-PiB) to allow for assessment of the degree of myelination of the lesions. Euthanasia and brain dissection were performed between one and seven days after the last imaging procedure. Note that due to the use of the radioactive ^{11}C-PiB tracer, dissection could not have been safely performed immediately after imaging.

Preparatory imaging

CT scans were performed on a Siemens Symbia T6 scanner without contrast medium or intravenous contrast material. They were essential for planning the surgical trajectory through the skull and the wide frontal sinuses of the minipigs. CT-image data were acquired in helical mode with a peak tube voltage of 130 kVp and a slice thickness of 1.25 mm. To avoid injuring macroscopical arterial and venous blood vessels during injections, and because the risk of injury would be insufficiently detected with the CT scans only, we performed an intravenous contrast medium–enhanced MRI (Gd-MRI), undertaken using a field strength of 3T (Siemens Biograph mMR) and consisting of contiguous 0.5 mm T1 and 0.8 mm MPRAGE (Gd) sequences of a volume which included the skull and the whole snout of the animal (Fig. 1a and c).

Lysophosphatidylcholine preparation

Lyophilised lysophosphatidylcholine (Fig. 1b) in powder formulation (LPC, Sigma Aldrich) was dissolved in iso-osmolar phosphate-buffered saline (PBS) at 40 °C achieving a concentration of 20 mg/ml. The solution was aliquoted and stored at –20 °C, then thawed before use. As a control, we used sterile PBS.

Injection system

To achieve efficient (reflux-free) and precisely placed and dosed convection-enhanced delivery (CED)[25] of LPC or PBS, we designed an electromagnetic tracking system (described in a subsequent section) with a compatible cannula (Fig. 2a and b). The cannula had a rounded tip, was made of stainless steel and featured a 3D-printed biocompatible Luer-Lock fitting (Fig. 2c and d). It had an outer diameter of 2.0 mm, an inner diameter of 0.85 mm, and a total length of 250 mm and was designed to accommodate 20 G epidural catheters (Braun Perifix, Germany). To track and visualise the cannula via the navigation system, we inserted a sensor wire, designed and manufactured by us, into the cannula and connected it to the Luer-Lock fitting (Fig. 2b and c). The sensor wire had a diameter of 0.8 mm and was inserted about 1 mm short of the tip of the cannula.

The injection cannula and the sensor wire were inserted with the aid of the robotic system mounted on the guide sleeve and controlled via a joystick by the operator. The robot was connected to the navigation system, receiving positional data to stop the injection cannula when the desired injection depth was reached. To minimise mechanical damage to the tissue at the injection site, we employed a 20 G epidural catheter that protruded around 3–5 mm from the tip of the cannula. In this way, we achieved a telescopic profile at the tissue-cannula interface, which has been shown to minimise reagent reflux[26] (Fig. 2d and e; Supplementary Video S1). 250 µl of LPC (intervention hemisphere) or PBS (control hemisphere) were injected over 50 min (5 µl/min) using a Harvard microinjector (Harvard Pump 11 Elite, Harvard Apparatus, USA). The injection cannula was then maintained in place for 10 min after complete reagent delivery (total tissue insertion time 60 min) (Fig. 2f). The slow injection rate was necessary to allow for diffusion in the cerebral parenchyma and to avoid significant reflux of reagent.[25]

Navigation system

The navigation software we developed (Drug Delivery V6.3.1) supported importing and fusing the CT and MRI data, planning trajectories and entry points, surface registration and real-time visualisation of instruments/cannulas in canonical planes, and 3D segmentations.

The navigation system that we designed and fabricated consisted of a processing unit/panel PC running our navigation software, which was connected to an
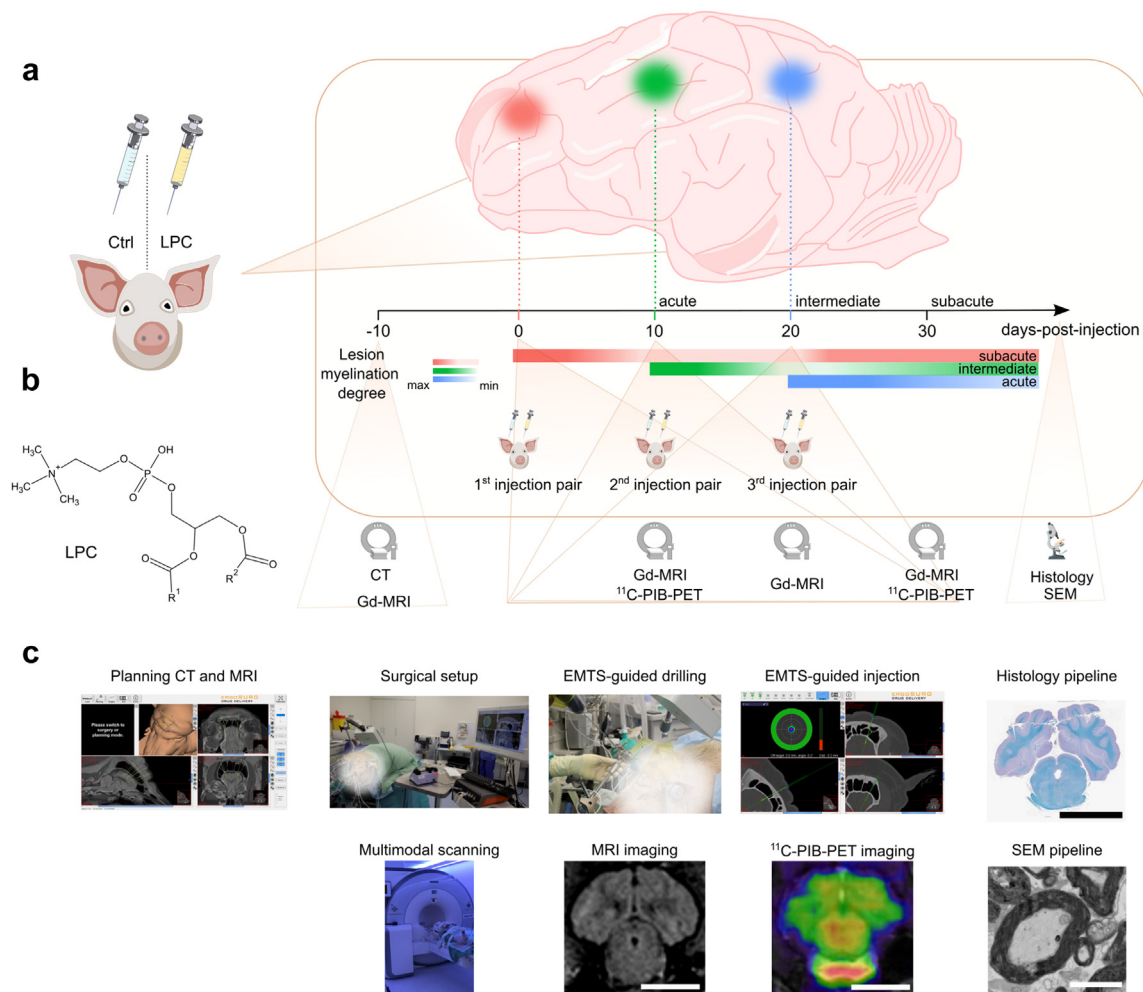
Fig. 1: MiniSWINE methodology overview. a) Demyelination induction and remyelination follow-up timeline (d = days). Timepoint "0": baseline imaging using CT and Gd-MRI. Timepoints "10-20-30 days post-injection": every ten days induction of a new demyelinating lesion at a distinct localisation in the centrum semiovale and follow-up of the previous lesions. Gradient colour schematic reflects successive de- and remyelination stages. SEM = scanning electron microscopy. b) LPC chemical formula; R^1, R^2 = variable fatty acid chains. c) Overview photographs and photomicrographs of successive stages of *MiniSWINE*. White blurring obscures content with potentially strong emotional impact. The scale bar in insets "MRI imaging", "^{11}C-PIB-PET imaging", and "Histology pipeline" is 25 mm, and the scale bar in inset "SEM pipeline" is 2.5 μm. EMTS = electromagnetic tracking system.

electromagnetic tracking unit, ETU (Fig. 2a). In its electromagnetic field, the position and orientation of instruments with integrated sensors connected to the ETU could be measured once a registration process was completed. The registration required a reference point with a fixed position relative to the minipig's head, for which we firmly attached a reference tracker to the head via the holding arm (Fig. 2b). The registration itself was based on surface matching, where the system measured the tip of a navigation probe with which the operator touched salient surface features of the minipig head, that were then matched to the image data by our software (Supplementary Video S2). This surface matching took 15 ± 0.1 s *in vitro* (for 110 points) and 96 ± 4.4 s

in vivo (for 482 points), thus not significantly impacting surgical time.

To guide the drill and the injection cannula, we attached a guide sleeve to another holding arm, which carried a sleeve tracker for precise alignment. The guide sleeve with its 6 degrees of freedom (DoF) tracker (Fig. 2b) was positioned by the holding arm attached to the Mayfield clamp supporting the head of the minipig. A custom-made cannula with a Luer-Lock fitting was fabricated. For navigating the cannula, we fabricated a so-called sensor-wire, a superelastic nickel-titanium alloy wire with a 5 DoF sensor in the tip, which could be inserted into the cannula and attached via the Luer-Lock fitting (Fig. 2c).
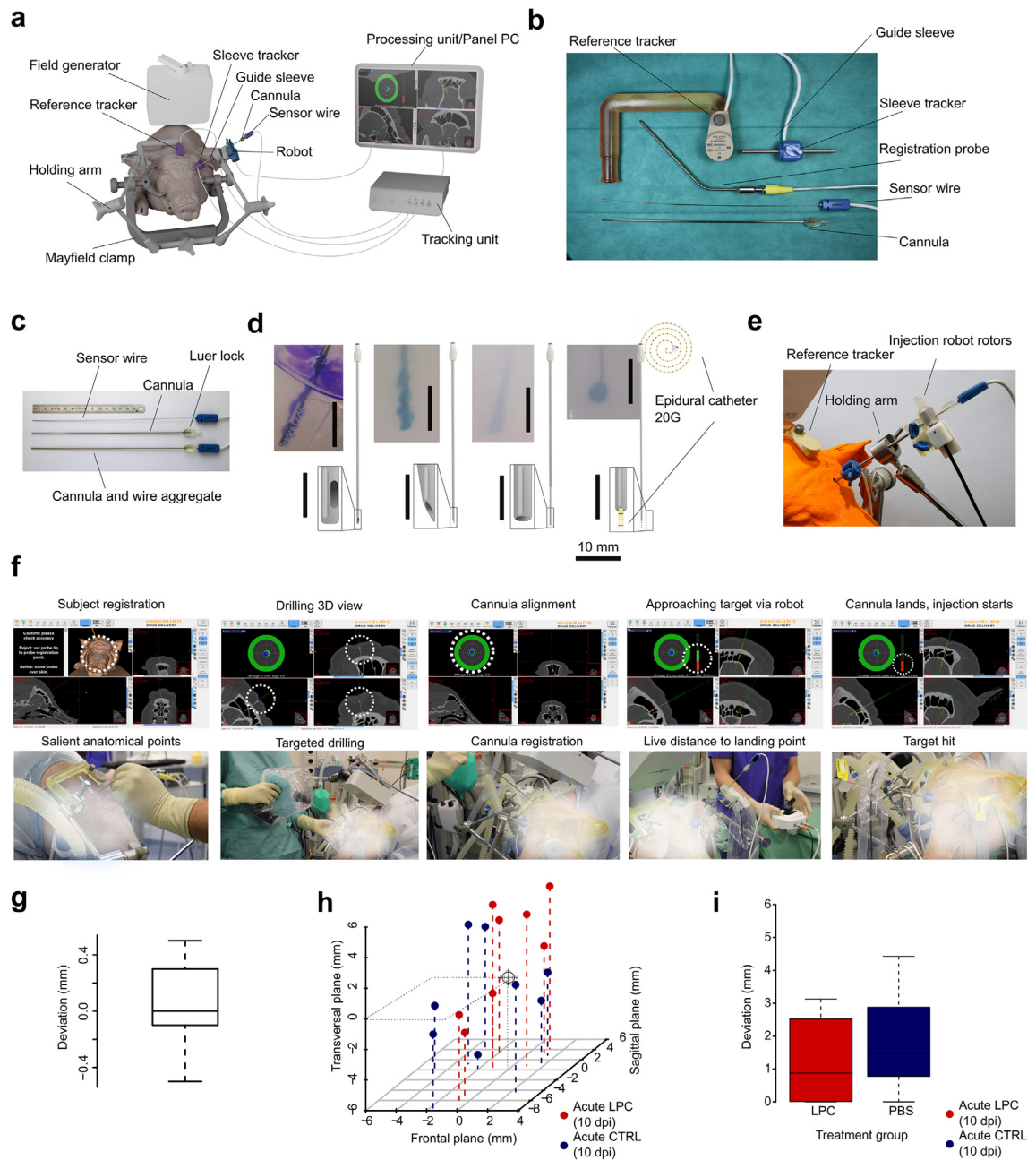
Fig. 2: MiniSWINE: electromagnetic-tracking system (EMTS) and surgical procedure. a) *MiniSWINE* setup for EMTS. b) The reference tracker was rigidly attached to the minipig forehead. The tracked guide sleeve was essential for the precise alignment of the drill. c) Cannula assembly. The CED cannula was trackable as long as it contained the sensor wire. Once on target, the wire was replaced with the single-use 20G epidural catheter. d) Sequential cannula development, cannula tip profiles, and empirical spread functions of CED in 0.2%–0.6% agarose gel. Evolution from a modified human brain biopsy cannula with a side-opening near the tip (far left) up to our definitive "telescopic" design (far right) with a round bevelled edge. Notice the near-ideal spherical spread function of the latter. e) Injection "hands-on" robotic system assembly consisting of a control unit and a small robot for the controlled and tracked insertion of the cannula. f) *MiniSWINE* software in operator view, 1st row and corresponding surgical overview, 2nd row. White dotted circles in 1st row mark system feedback to the operator. White blurring obscures content with potential emotional impact. g) Mean *in vitro* deviations from the target in a phantom test of 0.23 ± 0.03 mm (n = 25 trials). h) Scatterplot of 3D deviations from target *in vivo* in all 3D planes; black "target" set in the common origin of the coordinate system. i) Mean *in vivo* deviations from the target by study group: no significant difference between acute LPC lesions (1.24 ± 0.5 mm, n = 8) and acute CTRL lesions (1.83 ± 0.5 mm, n = 8), 1-way ANOVA with *df* = 1, *F* = 0.71, *p* = 0.41.

The sensor wire also measures the bending and defects of the cannula. The sensor clip helps to align the guide sleeve with the planned trajectory and entry point. The medical robot controls the insertion of the cannula along the trajectory. A reference tracker is rigidly attached to the subject's head to provide a fixed reference point for navigation. The navigation software displays the imaging data, the 3D model of the brain, and the feedback on the cannula position and orientation on a screen during the surgery. The navigation system works as follows:

- Before the surgery, the navigation software imports and fuses the CT and MRI data of the subject's brain.
- The navigation software allows the planning of the injection trajectories and entry points based on the imaging data and the 3D model of the brain.
- During the surgery, the reference tracker is attached to the subject's head, and the electromagnetic field generator is positioned near the head.
- Using a probe connected to the electromagnetic field generator, the navigation software registers the subject's head surface and landmarks, such as the nasal ridge, frontal bone, zygomatic arcades, and mandibular joints.
- The sensor clip is attached to the guide sleeve, and the sensor wire is inserted into the cannula. The sensor clip and wire are connected to the electromagnetic field generator.
- The navigation software tracks the position and orientation of the sensor clip and wire. It visualises both on the screen relative to the imaging data and the 3D model of the brain.
- The sensor clip is used to align the guide sleeve with the planned trajectory and entry point under the guidance of the navigation software.
- The medical robot controls the insertion of the cannula along the trajectory. At the same time, the navigation software provides real-time feedback on the cannula's position and orientation and detects any bending or defects of the cannula.

Surgical procedure

The basic anaesthesia regime for both surgeries and imaging included sedation by combining ketamine 15 mg/kg body weight (bw), azaperone 2 mg/kg bw and atropine 0.1 mg/kg bw intramuscularly. An intravenous catheter was placed in the lateral auricular vein. Induction of anaesthesia was performed by infusing propofol (ca. 4–8 mg/kg bw titrated to effect) intravenously (IV) to achieve an adequate depth of anaesthesia for oral intubation with a 5–7 mm cuffed endotracheal tube. Anaesthesia was maintained by a continuous IV infusion of propofol 2% (ca. 2.5–7 mg/kg bw/h). Minipigs were mechanically ventilated in volume-controlled mode and oxygenated with 1–2 L O_2/min, mixed with 1 L

atmospheric air/min. Tidal volumes (ca. 10 ml/kg) and breathing rate (ca. 12/min) were adapted to the end-tidal CO_2. Positive end-expiratory pressure (PEEP) was kept at 5 mmHg. Saline was infused IV at a maintenance rate of ~10 ml/kg/hour. Intraoperative monitoring included reflex status, heart rate, peripheral arterial oxygen saturation (SpO_2), end-tidal carbon dioxide (ET-CO_2) and body temperature using an electrocardiogram, pulse oximeter, and rectal thermometer. External warm-air supply was provided. A single-shot Cefuroxim IV (500–750 mg) was administered before the skin incision. For multimodal analgesia during the surgery, metamizole (50 mg/kg bw), carprofen (4 mg/kg bw) and fentanyl-boluses (0.001–0.01 mg/kg bw) were administered IV every 20–30 min. For the imaging procedure, a second peripheral venous catheter was placed into the antebrachial or cephalic vein to administer the radioactive tracer.

Minipigs' heads were positioned and fixed in a Mayfield clamp (Pro Med Instruments, Freiburg, Germany), then shaved and disinfected at the operative situs (Fig. 2a and f). Using the tracker, the surface of the skull was registered and thus digitally superimposed on the planning imaging dataset (a fusion between CT and MRI) (Supplementary Video S2). The trackable guide sleeve was aligned to the planned trajectory and fixed in place. A 2.6 mm-wide burr hole trepanation was drilled through the lamina externa and interna of the frontal bone until the dura mater (haptic loss of resistance) was reached (Fig. 2f, Supplementary Video S3).

Then, a medical robot was attached at the entry of the guide sleeve, and the injection cannula and the sensor wire were inserted manually into the robot and the guide sleeve. With the navigation system's feedback, the robot inserted the cannula into the brain and stopped automatically when the intended intraparenchymal target was reached (Supplementary Video S2). Finally, the sensor wire was removed and replaced with the 20 G epidural catheter, through which, after connection to the Harvard microinjection pump, LPC or PBS was infused.

We aimed the three successive LPC/PBS injections in the same minipig brain to be at least 5 mm apart along a rostrocaudal axis in the centrum semiovale of both hemispheres. The mean injection coordinates, subsequently assessed based on MRI data, computed with the vertex as a reference were: −2.8 ± 0.7 mm and 13.2 ± 2.2 mm in the axial plane (intervention and control), −3.6 ± 1.7 mm in the coronal plane and, for the first pair of injections: −53.1 ± 1.8 mm, the second pair of injections: −41.9 ± 0.6 mm, and the third pair of injections: 35.62 ± 1.1 mm in the sagittal plane. After injection, the incision was sutured. The total surgical time amounted to approximately 3 h, from which approximately 30 min were required to fix the head in the Mayfield clamp and for navigation and 2 h for injection time. Postoperative analgesia was administered as daily carprofen per os or intramuscular (4 mg/kg bw)

over five days, as well as buprenorphine IM (0.01–0.1 mg/kg bw) for three days. Antibiosis was maintained in parallel with daily amoxicillin PO or IM (15 mg/kg bw). Veterinarian observations were performed once daily for the entire experimental duration to ascertain that the animals did not develop any signs of neurological deficits due to the intracerebral injections.

Longitudinal MRI imaging

Minipigs were placed in a 3.0 T Siemens Biograph mMR (Siemens, Germany) with the head fixed in a standard cage head coil. In agreement with the 2021 MAGNIMS consortium[27] recommendations on the use of MRI in patients with MS and the 2017 McDonald criteria[28] for the diagnosis of MS, we performed sagittal 3D T2-weighted (1.5 mm slice thickness, echo time = 107 ms, repetition time = 4220 ms), sagittal and axial isotropic 3D T2FLAIR (1 mm slice thickness, echo time = 393 ms, repetition time = 6000 ms, inversion time = 1800 ms), T1-weighted post-contrast/T1Gd (contrast medium: Gd, Dotagraf, 0.5 mmol/ml, 2 mm slice thickness, echo time = 2.84 ms, repetition time = 250 ms), T1-weighted magnetisation-prepared rapid acquisition with gradient echo (MP-RAGE)[29] (1 mm slice thickness, echo time = 3.13 ms, repetition time = 1920 ms, inversion time = 999 ms), double-inversion recovery for detecting potential juxtacortical lesion extensions (DIR, 1 mm slice thickness, echo time = 318 ms, inversion time = 3000 ms, repetition time = 7500 ms), and T1-weighted "black-blood" (slice thickness = 0.5 mm, echo time = 11 ms, repetition time = 1070 ms). To the MRI scan protocol derived from the MAGNIMS criteria, we added SWI (susceptibility-weighted imaging, slice thickness = 9.6 mm, echo time = 20 ms, repetition time = 28 ms) sequences, which are particularly sensitive to iron content from venous blood and haemorrhage to ascertain that tissue changes after LPC/CTRL-injections are not due to injection-induced bleeding.

MRI image analysis

The images were processed with the MITK Workbench v2018.04.2 software (https://www.mitk.org) using its 3D segmentation toolbox. Regions of interest (ROIs) were semi-automatically segmented in T2FLAIR, T1Gd and SWI sequences, and their volumes (in mm^3), excluding the injection trajectory path, were quantified. Volumes from the LPC injection site were compared to the contralateral PBS injection. Deviations from the lesion targets were determined via automatic superposition of CT and MRI data obtained at baseline and after injection, from which the mean superposition imprecision between the CT and MRI datasets was subtracted. The superposition imprecision was determined at the midpoint of the sphenoid bone ridge, reliably identifiable in CT and T1 MRI.

As SWI hyperintensity might correspond to microhaemorrhage along the injection trajectory as seen in patients referred for neurosurgery,[30] we excluded from the analysis lesions with a volume of SWI hyperintensity higher than 100 mm^3, a threshold based on the calculation of the volume ($V = \pi \times r^2 \times h$) of the lumen of the cannula (inner diameter = 0.8 mm = 2 × r; length = 250 mm = h). For every lesion, we calculated the volume after segmentation in the T2FLAIR sequences and derived the diameter of a sphere of equal volume.

Longitudinal PET imaging

To the standardised MRI protocols, we added a diagnostic method under development, with potential for the specific quantification of de- and remyelination *in vivo* and, therefore, evaluation of future remyelinating treatments, which is PET employing WM-binding tracers, such as the thioflavin-T derivative 2-(40-methylaminophenyl)-6-hydroxybenzothiazole (Pittsburgh compound B, PIB), pioneered in a proof-of-concept study on two patients with MS.[31] We produced it according to standard protocols.[32,33] Animals were injected through an intravenous catheter placed in the lateral auricular vein with approximately 370 MBq of ^{11}C-PIB. Between 45- and 60 min post-injection, a 15-min list-mode scan was acquired in 3D mode on a Siemens Biograph mMR scanner. Emission sinograms were reconstructed using ordered subset expectation maximisation (OSEM), corrected for attenuation, scatter, randoms, dead time, and radioactivity decay and smoothed using a Gaussian kernel. Mean standardised uptake values (SUV) were calculated by area-weighted averaging and compared between the LPC and PBS injection sides using the software Weasis v.3.8.1 (https://nroduit.github.io/en/) after a slice-by-slice manual delineation of the lesion volumes in the overlapped PET/MRI datasets.

Histopathology and immunohistochemistry

We performed histopathology and immunohistochemistry on the brains of animals that were euthanised by pentobarbital overdose in deep anaesthesia, 49 ± 7 days after the initial pair of intracerebral injections. We fixed the dissected brains in 4% PFA at 4 °C for 60 days by submersion and embedded them in paraffin wax according to previously published procedures.[34] We cut the cooled (4 °C) paraffin blocks in coronal orientation at 4–5 μm thickness using a semiautomated rotary microtome (Leica, Germany) and mounted the sections on slides.

For histopathological staining, we rehydrated the sections by incubating them in decreasing ethanol concentrations, from 100% to water. We performed antigen retrieval in antigen retrieval buffer solutions (Biolegend) for 15–20 mins at 90 °C. We stained the sections with Luxol fast blue (LFB, Klüver-Barrera)—periodic acid-Schiff (PAS) or haematoxylin and eosin (H&E). For LFB-PAS staining, we incubated the sections in an LFB solution for 6 h at 56 °C and differentiated

them in 0.05% lithium carbonate. We then incubated them in Schiff's Reagent (Sigma) for 15 min at room temperature (16–25 °C) and counterstained them with haematoxylin solution, Gill No. 3 (Sigma-Aldrich), for 90 s. For H&E staining, we counterstained the sections with haematoxylin for 5 min and eosin for 1 min. We cleared the sections with xylene and mounted them with mounting media.

For chromogenic immunochemistry, we cut 2 μm thick slides with a standard microtome and dried them at 76 °C for 30 min. We used a fully automated staining system (BOND-III; Leica Biosystems, UK) to perform immunostaining for glial fibrillary acidic protein (GFAP), ionised calcium-binding adaptor molecule 1 (Iba1), oligodendrocyte transcription factor 2 (Olig2), neuronal nuclear antigen (NeuN), cluster of differentiation 3 (CD3) and cluster of differentiation 68, CD68. The system used the BOND Polymer Refine Detection Kit (Leica Biosystems, UK) for antibody detection and counterstaining, which contains a post-primary IgG linker reagent and a poly-HRP IgG reagent for the localization of mouse and rabbit antibodies, respectively. The system also utilizes a polymerization technology to prepare polymeric HRP-linker antibody conjugates. We pretreated the slides in pH 8.4 buffer for heat-induced antigen retrieval and in 3% H_2O_2 to inhibit endogenous peroxidase for 10 min. We then incubated the slides with the following primary antibodies: anti-GFAP (monoclonal, rabbit, dilution 1:500; Cell Marque, Rocklin, CALIF, USA), anti-Iba1 (polyclonal, mouse, dilution 1:1000; Fujifilm Wako, Japan), anti-Olig2 (monoclonal, mouse, ready to use; Cell Marque, Rocklin, CALIF, USA), anti-NeuN (monoclonal, mouse, dilution 1:1000; Cell Marque, Rocklin, CALIF, USA), anti-CD3 (monoclonal, rabbit, ready to use; Roche, Switzerland), or anti-CD68 (monoclonal, mouse, dilution 1:200; Cell Marque, Rocklin, CALIF, USA).

For immunofluorescence, we deparaffinised and rehydrated the slices by immersing them in xylene and a series of solutions of decreasing ethanol concentrations. We performed antigen retrieval with the All-Antigen Unmasking Kit (Bio Legend) following the manufacturer's protocol. We blocked the sections with 5% goat serum for 2 h at room temperature. We then incubated them overnight with primary antibodies against GFAP (Cat#13-0300, ThermoFisher), MOG (Cat#MAB5622, Merck Millipore) and NFH (Cat#AB5539, Merck Millipore). We incubated the slides in secondary antibodies at room temperature for 1 h. We used Alexa Fluor 555 nm labelled goat anti-mouse secondary antibody (Cat#A28180, ThermoFisher) against MOG, Alexa Fluor 488 nm labelled goat anti-rat secondary antibody (Cat#A11006, ThermoFisher) against GFAP and Alexa fluor 488 nm labelled goat anti-chicken secondary antibody (Cat#A11039, ThermoFisher) against NFH, all at a dilution of 1:200. We mounted the sections with Prolong Gold Antifade mounting media with DAPI (Invitrogen), examined them under a confocal microscope (Olympus FV1000), and scanned them using Olympus Fluoview Software.

We examined the slides from histopathology and chromogenic immunohistochemistry under a bright field microscope (Leica, Germany) and scanned them using a microscope-mounted camera. We uploaded the images to the PathoZoom Slide Cloud (https://www.pathozoom.com/) and processed them using Fiji ImageJ (https://imagej.net/software/fiji/).[35] We quantified the demyelination areas in the LFB-stained slides and compared them between the intervention (LPC) and control (PBS) study groups from lesions of the same stage. We also quantified the cell densities of Olig2+, NeuN+ and CD3+ per $300 \times 300\ \mu m^2$ ROI, and the proportions of astrocytes and microglia per $1 \times 1\ mm^2$ ROI, in the immunohistochemistry slides. We did not quantify the CD68 staining due to the low signal-to-noise ratio, which we attributed to species cross-reactivity.

We calculated the demyelination areas by manually tracing each section obtained per lesion using Image J and summing the areas across sections. We used the following formula[36,37]:

$$A_k = \sum_{i=1}^{n} \sigma_i$$

here, A_k represents the area of lesion k, n is the number of sections obtained for lesion k, and σ is the cross-section area in mm^2 of section i. We did not compute the volumes because multiplying the slice thickness and the section-by-section area would not provide any additional information (a derivative of a constant is null) but could introduce measurement errors due to variations in slice thickness or sampling.

Electron microscopy

Minipig brain, as well as human biopsy tissue used for the scanning electron microscopy (SEM) experiment, was immersed directly after dissection in fixative solution (2.5% glutaraldehyde, 4% paraformaldehyde in phosphate buffer, 2 mM calcium chloride, 0.1 mM cacodylate buffer). After fixation for 48 h at 4 °C, the lesion areas (intervention or control, same lesion stage) were washed in 0.1 M cacodylate buffer and dissected. We applied a standard reduced osmium-thiocarbohydrazide-osmium (rOTO) protocol *en bloc* staining[38] including postfixation in 2% osmium tetroxide (Science Services), 1.5% potassium ferricyanide (Science Services) in 0.1 M sodium cacodylate (Science Services) buffer (pH 7.4). Staining was enhanced by reaction with 1% thiocarbohydrazide (Sigma) for 45 min at 40 °C. The tissue was washed in water and incubated in 2% aqueous osmium tetroxide, washed and contrasted by overnight incubation in 1% aqueous

uranyl acetate at 4 °C and 2 h at 50 °C. Samples were dehydrated in an ascending ethanol series and infiltrated with LX112 (LADD). SEM was performed on 100 nm thick sections collected onto carbon nanotube tape (Science Services) and mounted onto a silicon wafer (Microchemicals). EM micrographs were acquired on a Crossbeam Gemini 340 SEM (Zeiss) with a four-quadrant backscatter detector at 8 kV. In ATLAS5 Array Tomography (Fibics), wafer overview images (1.5 µm/pixel), as well as medium (200 nm/pixel) and high (10–20 nm/pixel) resolution images, were acquired. Images were processed using the Fiji software, and a manual assessment of the degree of myelination in SEM images was made using the g-ratio, the ratio of the inner diameter of an axon to the outer diameter of the myelinated fibre.[39] Quantification was performed on 10–20 nm/pixel resolution images for the presence/absence of (myelinated) axons per area. We counted 1499 axons in the minipig subcortical WM across all disease stages and 1614 axons in the human samples.

Statistics

A minimal number of minipigs and induced lesions was predetermined by statistical power analysis. Considering a previously described intraindividual correlation of $r^2 = 0.85$ between imaging and tissue analysis in a rodent study,[40] we needed at least 3 animals with at least $3 \times 3 = 9$ samples for a two-sided statistical significance level of 5% ($\alpha = 0.05$). This number increases to 6, considering a drop-out rate of 50% described in the literature in large-animal studies.[41] Because of the repeated lesions in the same animals that were longitudinally followed up, we collected data from n = 22 lesions in 8 animals in the acute stage, from n = 12 lesions in 6 animals in the intermediate stage and n = 6 lesions in 5 animals in the subacute stage. The spatial and temporal separation of lesions allowed them to be regarded as independent statistical units. Statistical analysis was performed using the open-source software R (https://www.R-project.org/, version 4.1.0) and R Studio (version 1.4.1717). Data were tested for normality and equality of variance using the Shapiro–Wilk test and, respectively, the Bartlett test. If the data passed normality and homoscedasticity criteria, we performed one-way repeated-measures ANOVA tests with Bonferroni adjustments for multiple comparisons. If they did not, we performed the Kruskal–Wallis test with Dunn's multiple comparisons test. All statistical tests were two-sided and carried out to a significance level of $p \leq 0.05$. If not stated otherwise, reported values represent mean ± s.e.m.

Role of funders

Funders had no role in study design, data collection and analysis, interpretation of the data, or the reporting of the study.

Results

For the *MiniSWINE* methodology (Fig. 1a), we resorted to stereotactic microinjection of LPC (Fig. 1b) for optimal spatiotemporal control. We chose EMTS (Figs. 1c and 2a) over OTS, as EMTS does not require a visual axis (i.e., line-of-sight). Moreover, as EMTS does not rely on direct visualisation, handling the navigated drill guide on small surfaces such as the porcine forehead is easier. Finally, with EMTS navigation, the porcine head positioning in the clamp holder does not have to be adjusted intraoperatively.

Accuracy of the stereotactic navigation system

We empirically determined which cannula tip profile resulted in the optimal spread patterns of the injected substance by *in vitro* injections into 0.2% or 0.6% agarose gels (which have been described to imitate the consistency of the mammalian brain).[26,42] We tested volumes and infusion rates compatible with CED,[43] i.e., 250 µl at 5 µl/min. Known problems of the standard needle profiles used in stereotactic biopsy needles, which have a bevel or side aperture near the tip, are backflow and an elongated spread pattern along the needle tip. It has been shown that backflow can be influenced by the consistency and the profile of the needle tip.[44] Therefore, we custom-designed an autoclavable cannula with an outer diameter of 2 mm and a rounded tip (Fig. 2c), minimising haemorrhage risk. A standard single-use 20G silicon epidural catheter (0.85 mm outer diameter) could be inserted through this needle, replacing the sensor wire to protrude 3–5 mm from the tip. In this way, the needle tip was soft and exhibited a step profile, which has been described to minimise backflow issues.[44] Consequently, the spread functions reached elliptical/almost spherical shapes of at least 5 mm radius, which was the minimal spatial resolution of the PET scanner (Fig. 2d).

We developed a "hands-on" robotic system consisting of a control unit and a small robot for the navigated insertion of the cannula (Fig. 2e). The control unit was connected to the navigation system. It could be mounted on any operating table. The control unit had a joystick and a safety button to control the robot by navigation or hand, preventing unintentional activation. The robot was, in turn, connected to the control unit and could be mounted on the guided sleeve. It had two steel shafts with sterilisable silicone covers for inserting the navigated cannula into the brain via the guided sleeve. Only one of these shafts was motor-driven, so manual insertion or removal of the cannula was possible at any time.

Care was also taken to optimise the flow of the EMTS-assisted surgical procedure by quickly providing the essential visual feedback via our software in correspondence with the haptics sensed by the surgeon. After registration of the minipig head, we could visualise trackable instruments relative to the brain in presurgical CT and MRI image data in real-time in the

three orthogonal planes (axial, coronal, sagittal) and 3D segmentations. In addition, the software showed the remaining distance of the cannula's tip to the target. The trajectory planning could be done in the planning tool integrated into the navigation software or separately on a laptop or PC with the navigation software installed. To confirm registration accuracy, the surgeon touched the anatomical landmarks of the head with the probe's tip and checked the visualised position, revealing a registration error of 0.55 ± 0.01 mm *in vitro* and 0.87 ± 0.013 mm *in vivo*. To control the movement and insertion depth of the navigated cannula, the cannula was inserted into the guide sleeve and thus into the brain by the "hands-on" robotic system or manually by the surgeon. For the automatic insertion, the robot was also mounted to the sleeve and could move the cannula via its motor-driven shaft with a speed of 11 mm/s and a movement resolution of <0.1 mm. The surgeon could control the robotic system via the navigation software, which provided visual feedback of the remaining distance to the target on a screen for the operator and stopped the robot/the cannula's movement automatically as soon as the tip of the cannula reached the target (Fig. 2f, Supplementary Videos S1 and S3).

We tested the accuracy of the navigation system using a minipig phantom head and a 3D print of a CT dataset of one of our animals. In a typical operating room setup, the mean positional error of the system was 0.23 ± 0.03 mm (Fig. 2g). In our *MiniSWINE* brain surgery setting, the *in vivo* injection mean positional error was similar across the three orthogonal planes (Fig. 2h) and averaged 1.54 ± 0.4 mm over both study groups, with no statistically significant difference between LPC or CTRL (Fig. 2i). Given the spatial resolution of the detection systems (approximately 0.5 mm, see Methods), this imprecision was deemed acceptable.

MR-imaging

First, we investigated MRI signatures of the LPC-induced lesions on established protocols developed and used in clinical practice for patients with MS. We performed MRI imaging at intervals designed to capture critical stages in lesion evolution, as known from LPC-induced demyelination in rodent models[18] (Fig. 3a). We investigated an acute stage at a median of 9 days (IQR 7–14 days, n_{aLPC} = 22 aLPC lesions and n_{aCTRL} = 22 aCTRL lesions), an intermediate stage at a median of 20 days (IQR 19–23 days, n_{iLPC} = 12 iLPC and n_{iCTRL} = 12 iCTRL lesions) and a subacute stage at a median of 30 days (IQR 28–33 days, n_{sLPC} = 6 sLPC and n_{sCTRL} = 6 sCTRL lesions) after lesion induction. By longitudinal imaging in the same animal, lesions at earlier stages accumulated in higher numbers than lesions at the latter stages, so we obtained a 3:2:1 ratio between the number of acute, intermediate and subacute lesions in our study (Supplementary Figure S1).

We assessed T2FLAIR hyperintensity as a potential indicator of areas including demyelination. In the acute stage, LPC-induced lesions exhibited significantly larger volumes of T2FLAIR hyperintensity than their corresponding control lesions (aLPC = 535.1 ± 188.9 mm³ vs. aCTRL = 93.7 ± 63 mm³; Kruskal–Wallis test followed by Dunn's multiple comparisons test H(1) = 8.92, p = 0.003; Fig. 3b). This was corroborated by a statistically significantly higher volume of Gd uptake in T1 sequences in LPC lesions than in CTRL, suggestive of blood-brain-barrier breakdown in the acute stage (aLPC = 390.3 ± 96.7 mm³ vs. aCTRL = 31.7 ± 13.2 mm³; Kruskal–Wallis test followed by Dunn's multiple comparisons test H(1) = 11.84, p < 0.001; Fig. 3b). We also examined lesion signal intensity in DIR sequences when WM lesions were sufficiently close to the cortex to elicit juxtacortical demyelination potentially. LPC-induced lesions demonstrated statistically significantly larger volumes of DIR hyperintensity than their control counterparts (DIR: aLPC = 227.2 ± 94.7 mm³ vs. aCTRL = 12.1 ± 5.6 mm³; Kruskal–Wallis test followed by Dunn's multiple comparisons test H(1) = 11.31, p < 0.001; Fig. 3b). We included a 3D MP-RAGE sequence, a technique used to confirm the exact localisation (e.g., juxtacortical vs. cortical vs. mixed) of grey matter lesions in MS due to improved spatial resolution and signal-to-noise ratio compared to DIR[45] and confirmed statistically significantly larger hypointense signal volumes in the LPC lesions compared to control lesions (3D-MPRAGE: aLPC = 78.9 ± 46.0 mm³ vs. aCTRL = 3.9 ± 2.0 mm³; Kruskal–Wallis test followed by Dunn's multiple comparisons test H(1) = 4.66, p = 0.031) (Fig. 3b). However, we noticed no difference with respect to the volume of SWI hyperintensity between the LPC-induced and control lesions (aLPC = 48.6 ± 7.8 mm³ vs. aCTRL = 51.1 ± 7.6 mm³; one-way ANOVA followed by Tukey's multiple comparisons test F(1,25) = 0.11, p = 0.74) (Fig. 3b).

In the intermediate and subacute stages, we observed some return from the signal changes in the acute stage, suggesting restorative tissue changes that could include remyelination, as is the case in, for instance, rodent LPC models.[18] At the intermediate stage, while the volume of the T2FLAIR hyperintensity became similar in the LPC group to the CTRL group (iLPC = 189.0 ± 116.5 mm³, a 65%-decrease from aLPC vs. iCTRL = 30.7 ± 10.5 mm³, a 67%-decrease from aCTRL; Kruskal–Wallis test followed by Dunn's multiple comparisons test H(1) = 3.13, p = 0.07; Fig. 3b), there was still increased T1Gd uptake in the LPC group (iLPC = 152.0 ± 90.0 mm³, a 61%-decrease from aLPC vs. iCTRL = 6.1 ± 2.3 mm³, an 81%-decrease from aCTRL; Kruskal–Wallis test followed by Dunn's multiple comparisons test H(1) = 4.87, p = 0.03; Fig. 3b). In the subacute stage, no differences were detected between the LPC-induced and control lesions concerning T2FLAIR hyperintensity (sLPC = 46.4 ± 44.4 mm³ vs. sCTRL = 2.0 ± 2.0 mm³; Kruskal–Wallis test followed by
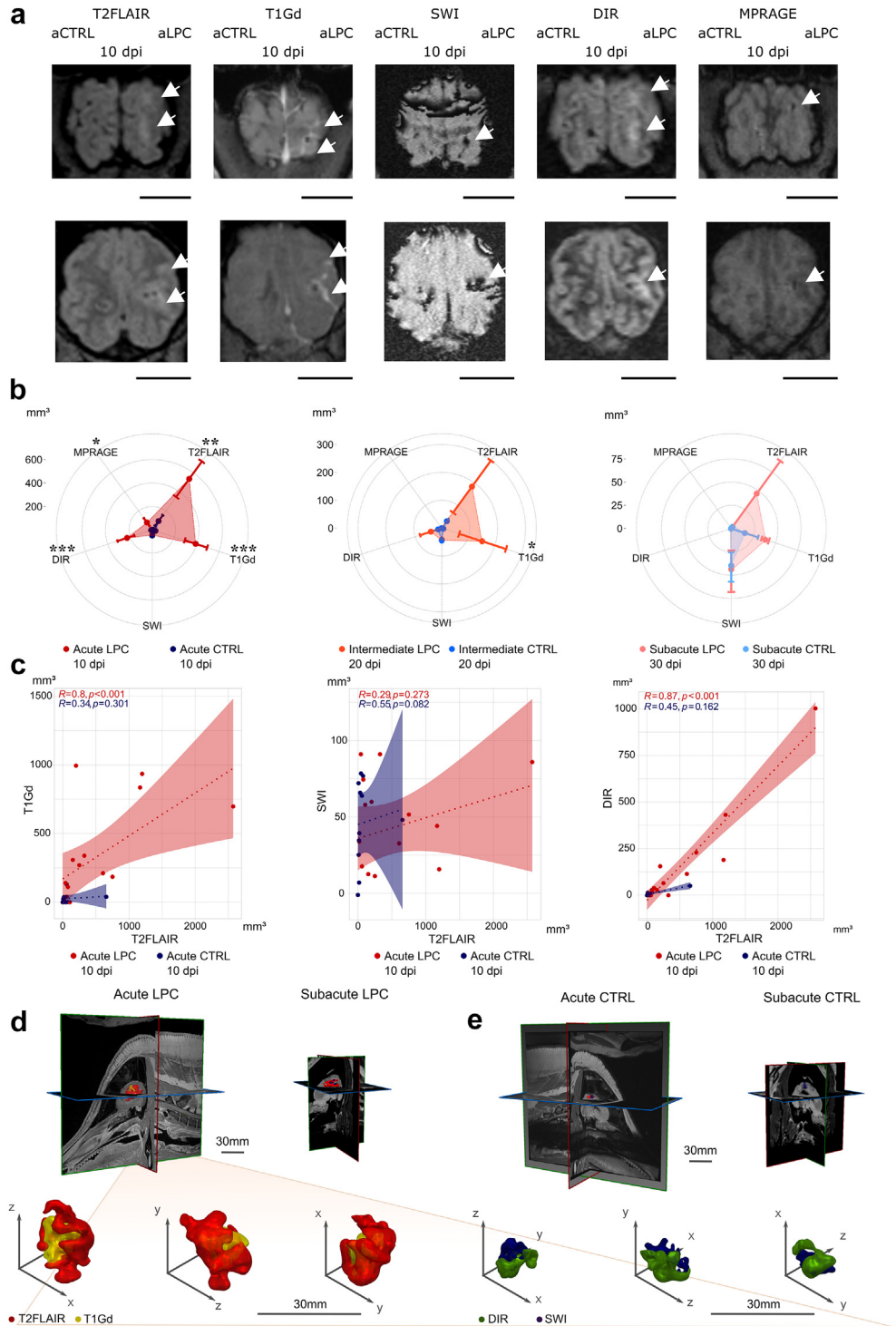
Fig. 3: MiniSWINE MRI. a) Example axial tomographic planes, each row corresponding to one acute lesion from a separate minipig, scale bar = 2 cm. b) MRI signals in each stage (*aLPC* n = 18, *aCTRL* n = 13; *iLPC* n = 11, *iCTRL* n = 9, *sLPC* n = 4, *sCTRL* n = 5). Statistical significance and *p* values were determined by the Kruskal–Wallis test followed by Dunn's multiple comparisons test, or, given data were normal and homoscedastic, by one-way ANOVA followed by Tukey's multiple comparisons test; *$0.01 \leq p \leq 0.05$, **$0.001 \leq p \leq 0.01$, ***$p \leq 0.001$. c) Spearman's correlograms between MRI signals: dotted lines for linear regressions, coloured areas for 95%-confidence intervals, R = Spearman correlation coefficient, *p* values from the Spearman's rank correlation test. d) 3D reconstructions of exemplary *aLPC*, and e) *aCTRL* lesions. Note that T2FLAIR hyperintense signals take up the largest volume, followed by T1Gd and, depending on the lesion localisation, DIR signals. In contrast, the SWI signals are mostly confined to the needle trajectory through the tissue.

Dunn's multiple comparisons test $H(1) = 0.48$, $p = 0.49$; Fig. 3b) and T1Gd uptake volumes ($sLPC = 38.4 \pm 4.2$ mm^3 vs. s$CTRL = 15.1 \pm 15.1$ mm^3; Kruskal–Wallis test followed by Dunn's multiple comparisons test $H(1) = 1.21$, $p = 0.27$) (Fig. 3b). In none of the other consensus MRI sequences (see above and Methods), neither at the intermediate, nor at the subacute stage, did we observe any significant signal differences between both groups.

Next, we evaluated the correlations between the T2FLAIR and T1Gd signals and between the T2FLAIR and SWI signals. In the acute stage, we observed a statistically significant positive correlation between T2FLAIR and T1Gd signal volumes in the LPC group (Spearman's $R = 0.8$, $p < 0.001$) but no significant correlation in the CTRL group (Spearman's $R = 0.34$, $p = 0.301$; Fig. 3c). Similarly, we found a statistically significant positive correlation between T2FLAIR and DIR signal volumes in the LPC group (Spearman's $R = 0.87$, $p < 0.001$; Fig. 3c), but not in the CTRL group (Spearman's $R = 0.45$, $p = 0.162$; Fig. 3b). Conversely when analysing T2FLAIR against SWI signal volumes, we found no correlation in the LPC group (Spearman's $R = 0.29$, $p = 0.273$; Fig. 3c) or the CTRL group (Spearman's $R = 0.55$, $p = 0.082$; Fig. 3c). Similar results were found at the intermediate stage. T2FLAIR and T1Gd volumes showed a significantly positive correlation in the LPC-induced lesions group (Spearman's $R = 0.64$, $p = 0.034$) but not in the control lesions group (Spearman's $R = 0.46$, $p = 0.214$), whereas T2FLAIR and SWI volumes exhibited no correlation in the LPC group (Spearman's $R = 0.4$, $p = 0.226$) or the CTRL group (Spearman's $R = 0.64$, $p = 0.064$) (Supplementary Figure S2). At the subacute stage, we observed no statistically significant correlations between T2FLAIR and T1Gd in both groups (Spearman's $R = 0.2$, $p = 0.917$) (Supplementary Figure S2). These results reinforced the hypothesis that the LPC-induced tissue effect, drove the MRI signal values in the treatment group at the acute stage. However, pending PET and ultrastructural validation, we could not ascertain that this effect was a demyelination. Conversely, we did not see any difference in the MRI signal kinetics that suggests different remyelination kinetics between different locations across the centrum semiovale, even though the MRI protocols we employed cannot be regarded as specific for myelination status. Therefore, we proceeded with a correlational analysis between imaging and histology.

In vivo PET-MRI and ex vivo histological analysis

We traced back tissue section locations by comparing anatomical landmarks in the histological slices to the coronal reconstruction of the MRI dataset (Fig. 4a). Specifically, the section-by-section alignment of ^{11}C-PIB-PET and T2FLAIR-MRI in vivo tomographic sections and Luxol fast blue (LFB)-stained and haematoxylin-and-eosin ex vivo tissue sections allowed to pinpoint the corresponding lesion locations across the different neuroimaging modalities and timepoints (Fig. 4b and c, Supplementary Figure S3). We confirmed demyelination by diminished Luxol fast blue staining (Fig. 4d–g) and myelin inclusions in PAS-stained macrophages[46] (Fig. 4h).

In the acute stage, all lesions from both the LPC-induced lesions group and the control group exhibited an equivalent sphere diameter of above 5 mm (Fig. 4i). By pooling lesions across all stages, we found a statistically significant inverse correlation between the T2FLAIR hyperintensity and ^{11}C-PIB standard-uptake-values corrected by weight ($SUVbw$) in the LPC-induced lesions group (Spearman's $R = -0.81$, $p = 0.027$), but not in the control group (Spearman's $R = -0.6$, $p = 0.35$), suggesting that at least part of the T2FLAIR hyperintense volume exhibited a reduced myelin content (Fig. 4j). Conversely, we could not determine any statistically significant correlation between SWI volume and ^{11}C-PIB $SUVbw$, neither in the LPC (Spearman's $R = -0.67$, $p = 0.102$) nor in the CTRL group (Spearman's $R = 0.5$, $p = 0.45$) (Fig. 4k). The pooled analysis of lesions across all stages was justified by the fact that T2FLAIR sequences cannot distinguish between de- and remyelination. We also demonstrated a statistically significant positive correlation between T2FLAIR hyperintensity volumes and demyelinated surfaces on LFB-stained brain slices in the LPC (Spearman's $R = 1$, $p = 0.017$) but not in the control group (Spearman's $R = 0.71$, $p = 0.182$) (Fig. 4l), supporting the hypothesis that demyelination processes drove the T2FLAIR signal changes in the acute stage.

On histological slices, slice-by-slice summation of segmented areas of reduced LFB-staining revealed a statistically significantly higher demyelinated area in the LPC group than in the control group for lesions at the acute stage ($LPC = 7.2 \pm 0.9$ mm^2, n = 4, vs. $CTRL = 0.3 \pm 0.3$ mm^2, n = 4; Kruskal–Wallis test $H(1) = 5.6$, $p = 0.018$). Conversely, partial remyelination (visually evaluated based on the intensity of LFB staining) was observed in the LPC but not in the CTRL group at the subacute stage ($LPC = 1.8 \pm 0.6$ mm^2, n = 4, vs. $CTRL = 0.1 \pm 0.1$ mm^2, n = 4; Kruskal–Wallis test $H(1) = 5.6$, $p = 0.018$; Fig. 4m). Remyelination rate was higher in the acute and intermediate stages than in the subacute stage (significant inverse correlation between remyelination surface and duration after lesion induction in the LPC, but not in the control group, Spearman's $R = -0.95$, $p = 0.051$, Fig. 4n).

Immunohistological and immunofluorescent characterisation

Although LFB provides specific myelin staining of brain tissue and can be used to track myelination status[47] reliably, the quantification of LFB-staining surface does not take into account the other cellular components of a lesion, such as oligodendrocytes, astrocytes, neuronal somata/axons, microglia/macrophages and
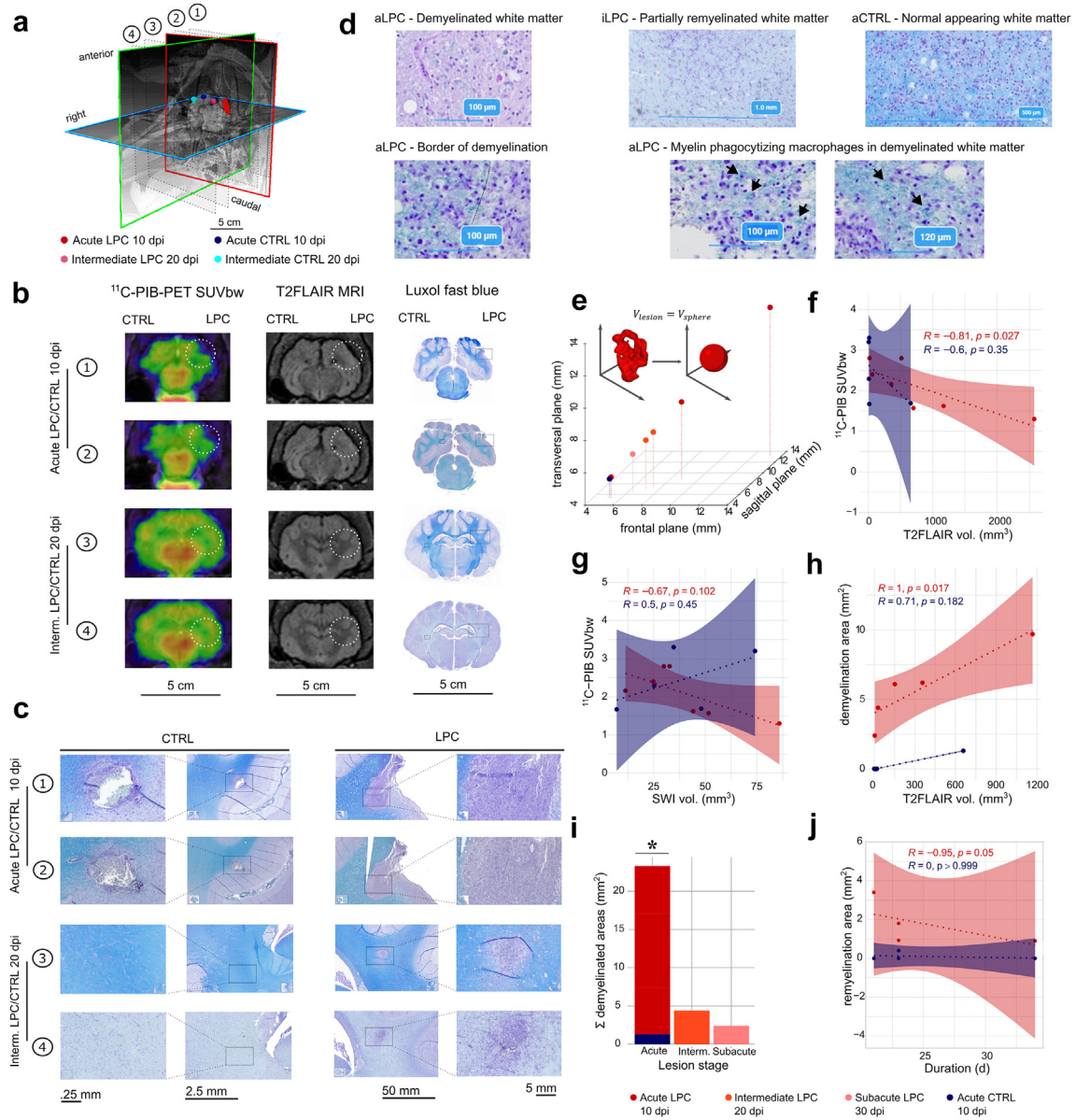
Fig. 4: Multimodal validation of de- and remyelination. a) Example 3D lesion reconstruction. Dotted planes correspond to localisations in the following: 1—*aLPC*, 2—*aCTRL*, 3—*iLPC*, 4—*iCTRL*. b) Correlative imaging and histopathology. Dotted white circles on PET/MRI correspond to black dotted rectangles in LFB photomicrographs. c) Higher magnification photomicrographs (note different scales for presentation purposes because LPC lesions are more extensive than CTRL) corresponding to the areas above. d) High magnification micrographs of exemplary aspects (from left to right): LFB-scarce WM in *aLPC*; partially, diffusely remyelinated WM in *iLPC*, corresponding to a region from c), rows 3–4; normal-appearing WM in *aCTRL*; well delineated (black line) border of demyelination in *aLPC*; additional indicators of fresh demyelination in the form of myelin phagocytosing macrophages (foam cells) in *aLPC*. e) Equivolumetric sphere size distribution for *LPC* (V = volume). f) Spearman's correlogram between the T2FLAIR volume and ^{11}C-PIB-uptake in *aLPC/aCTRL*. g) Spearman's correlogram between SWI susceptibility volumes and ^{11}C-PIB-uptake in *aLPC/aCTRL*. h) Spearman's correlogram between T2FLAIR volume and the histopathologically detectable mean demyelination areas in *aLPC/aCTRL*. i) Slide-by-slide sum (Σ) of demyelinated areas across groups. Statistical significance and p values determined by Kruskal–Wallis test followed by Dunn's multiple comparisons test, *$0.01 \leq p \leq 0.05$. j) Spearman's correlogram between time post-induction and mean remyelination area. R = Spearman correlation coefficient, p values are calculated from Spearman's rank correlation test.

lymphocytes. We, therefore, performed immunostaining of the following markers across all lesion stages: GFAP (for astrocytes), Iba1 (for microglia), Olig2 (for oligodendrocytes and OPCs), NeuN (for neuronal somata), CD3 (for lymphocytes) and CD68 (for macrophages), and double immunofluorescence of GFAP and MOG (for myelin) and NfH (axons) and MOG.

LFB demonstrated an area of focal demyelination in *aLPC* at the site of injection that appeared to exceed that of the control group, *aCTRL* (Fig. 5a and d, Supplementary Figure S4a). This was paralleled by dense immunostaining suggestive of cellular infiltration in *aLPC* consisting of CD3+ lymphocytes, GFAP+ reactive astrocytes, hypertrophic on visual examination, and Iba1+ activated microglia, visually imposing with hypertrophic cell bodies, amoeboid shape and thickened cellular processes (Fig. 5a and d). Overall, we observed few CD68+ monocytes/macrophages (Fig. 5a and d) but detected myelin-phagocytising ones in *aLPC* lesions (foamy cells) (Fig. 4h). The density of Olig2 immunostaining was reduced in *aLPC* lesions, but not in *aCTRL* (Fig. 5a and d and Supplementary Figure S4a). GFAP signal density was high. In contrast, MOG signal density was weak in *aLPC* lesions (Supplementary Figure S5a and d) but not in *aCTRL* (Supplementary Figure S6a). Reactive astrogliosis and activated microglia were still present in *iLPC* lesions, albeit less evidently than in *aLPC* lesions, and absent in *iCTRL* lesions (Fig. 5b and d, Supplementary Figure S4b). In *iLPC lesions*, we observed a dense CD68 immunostaining that appeared denser than in *aLPC* lesions, suggesting a higher density of CD68+ infiltrating cells. Variations in LFB staining and MOG-immunofluorescence were paralleled by variations in Olig2 immunostaining in the vicinity of the injection site (Fig. 5a–d, Supplementary Figure S5a–c), suggesting that demyelination occurred along with oligodendrocyte loss. At the same time, remyelination correlated with restoration of oligodendrocytes. The oligodendrocytes, however, did not restore levels in *sLPC* compared to the baseline (Fig. 5d).

NfH-immunostaining revealed irregular distribution of neurofilaments (Supplementary Figures S5a–c and S6a–c) in LPC lesions at all stages, which was not observed in CTRL lesions. We did not find reduced neuronal somata in the cortical regions adjacent to the WM where the injections were placed in *LPC* compared to *CTRL* lesions across all stages (Fig. 5d). However, exact correspondence between the adjacent cortical areas where neuronal somata were counted and the precise axons contained in the WM tracts affected by the lesions is not a given in this setting, so that we resorted to clarify this question ultrastructurally.

Corroboration via electron-microscopy and comparison with human data

We performed scanning electron microscopy (SEM) in both the LPC and CTRL groups at acute and subacute stages (*aLPC*, *aCTRL*, *sLPC*, *sCTRL*). Moreover, we compared these SEM minipig brain data with SEM biopsy data from two patients diagnosed and treated in our neurology department: Patient A with an acute MS lesion in a demyelinating stage (*aHum*) and Patient S with a subacute ADEM lesion in a remyelinating stage (*sHum*).

The *aCTRL* and *sCTRL* WM samples featured an abundance of axonal fibres with intact myelin sheaths (Supplementary Figure S7). In *aLPC* and *aHum*, we found that the axons exhibited features of pathological myelin: the myelin sheath was very thin, and we noticed myelin fragments in the extracellular space or intracellularly within lysosomal inclusions of phagocytising cells (i.e., foamy cells). In *aLPC*, we also observed phagocytes engulfing myelin sheaths (Fig. 6a). The latter two features were absent in *sLPC* or in *sHum*, in which we noticed thinly, incompletely remyelinated axons (Fig. 6a). Intracellular lipid droplets appeared localised within phagocytes (macrophages or microglia) in *aLPC*, while in *aHum* they were more frequent within astrocytes (Fig. 6a). Axonal diameter was lowest in the acute stage (*aLPC* = 0.115 ± 0.01 µm, n = 746; *aLPC* < *aCTRL*, Kruskal–Wallis test followed by Dunn's multiple comparisons test $H(1) = 32.90$, $df = 5$, $p < 0.001$), showed intermediate values in the subacute LPC lesion (*sLPC* = 0.22 ± 0.01 µm, n = 239; *sLPC* < *sCTRL*, Kruskal–Wallis test followed by Dunn's multiple comparisons test $H(1) = 14.08$, $df = 5$, $p < 0.001$, *sLPC* < *aCTRL*, Kruskal–Wallis test followed by Dunn's multiple comparisons test $H(1) = 12.34$, $df = 5$, $p < 0.001$) and exhibited higher values both in the acute control and subacute control groups (axonal diameter: *aCTRL* = 0.444 ± 0.01 µm, n = 426; *sCTRL* = 0.653 ± 0.02 µm, n = 239) (Fig. 6b). The variation of axonal diameter across stages in the minipig brain was consistent with reports in patients with acute and subacute MS lesions,[48] being in line with the measures of axonal diameter in our patients, which was lower in the patient in the acute stage than in the patient in the subacute stage (Patient A: *aHum* = 0.160 ± 0.01 µm, n = 1095, vs. Patient S: *sHum* = 0.301 ± 0.01 µm, n = 519) (Fig. 6b). We also quantified the g-ratio at 10 nm-resolution, defined as the ratio of the axon diameter to the diameter of the axon plus the myelin sheath, a higher g-ratio indicating a thinner myelin sheath. The g-ratio was highest in the acute LPC lesion (*aLPC* = 0.799 ± 0.01, n = 746; *aLPC* > *aCTRL*), took an intermediate value in the subacute LPC lesion, potentially supporting the evidence of thinly and incompletely myelinated axons (*sLPC* = 0.708 ± 0.01, n = 327; *sLPC* > *sCTRL*, *sLPC* > *aCTRL*, *aLPC* > *sLPC*), and exhibited lower values in the CTRL groups (g-ratio: aCTRL = 0.637 ± 0.01, n = 426; *sCTRL* = 0.626 ± 0.01, n = 239). The patient data had a similar relationship regarding g-ratios (Patient A: *aHum* = 0.697 ± 0.01, n = 1095, vs. Patient S, *sHum* = 0.612 ± 0.01, n = 519) (Fig. 6b).

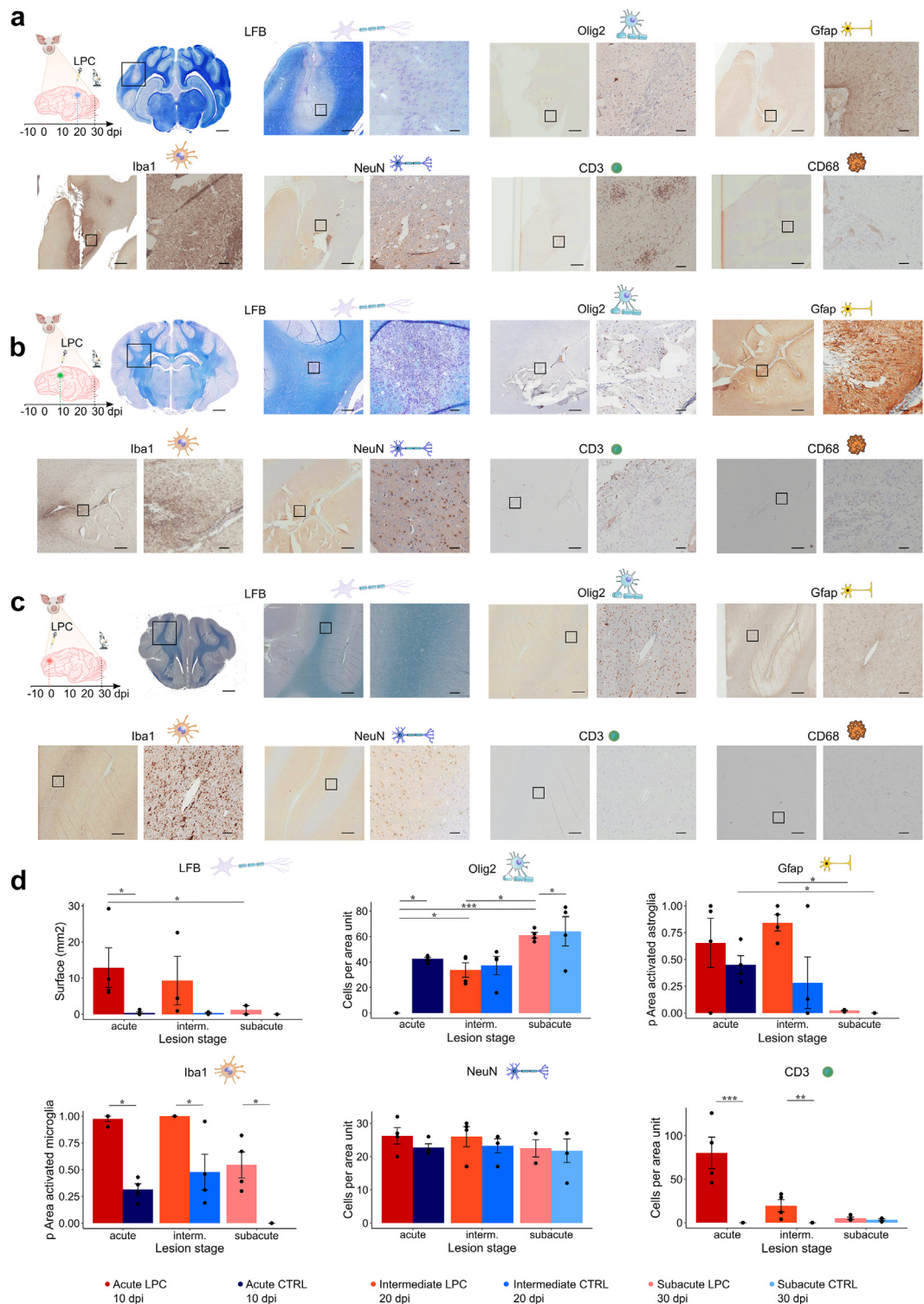We also consistently observed an increased proportion of pathological axons (thinly myelinated and

Fig. 5: Immunohistochemical characterisation of LPC lesions across stages. a) Acute stage (*aLPC*), b) Intermediate (*iLPC*), c) Subacute (*sLPC*). Common denominators of a–c): From left to right: Schematic corresponding to Fig. 1 of the lesion stage; LFB (Luxol fast blue) overview of the entire coronal slice (scale bar = 5 mm, black square delineates ROI magnified on the right and in each low magnification inset of the following stainings). Cell-specific marker stainings containing paired low-magnification (15×, left, scale bar = 1 mm, black square delineates ROI magnified on the right) and high magnification insets (right, 60×, scale bar = 100 μm) for following cellular markers: Olig2 (oligodendrocyte lineage cells),

demyelinated axons) in *aLPC*. In the former case, demyelinated axons were more frequent, while in *sLPC*, thinly myelinated axons were more frequent, even though the disproportion was not significant when compared to *sCTRL* (Fig. 6c). At the acute stage, the proportion of pathological axons over all axons was higher in *aLPC* (24% thinly myelinated, 5% demyelinated) than in *aCTRL* (8% thinly myelinated, 0% demyelinated). In comparison, in the subacute stage, the proportion of thinly myelinated axons over all axons was higher in *sLPC* (2% thinly myelinated) than in *sCTRL* (0.6% thinly myelinated) (Fig. 6c). Overall, we found a slightly lower density of axons in *sLPC* compared with *sCTRL* (by around 15%, axon density per $10 \times 10\ \mu m^2$ ROI: $sLPC = 25 \pm 3.5$, $sCTRL = 28.83 \pm 3.44$, $sLPC < sCTRL$, Kruskal–Wallis $p = 0.01$) (Fig. 6c). Together with data from NfH immunostaining, this hinted to a certain degree of secondary axonal degeneration present at the subacute stage.

By adjusting linear models to the distributions of axonal diameter and g-ratios from minipig and human tissue and performing likelihood ratio tests (LR), we could further corroborate the modelling of *aHum* data by *aLPC* regarding both axonal diameter (*aLPC* significantly improving LR over *aCTRL*, $Df = 3$, $H^2 = 263.83$, $p < 0.0001$) as well as g-ratio (*aLPC* significantly improving LR over *aCTRL*, $Df = 3$, $H^2 = 676.67$, $p < 0.0001$). Analogous results were obtained for approximating *sHum* by *sLPC* vs. *sCTRL* regarding the axonal diameter and the g-ratio (Fig. 6d). Thus, minipig LPC tissue exhibited similarities in key features of de- and remyelination stages to human inflammatory demyelinating CNS disease tissue regarding ultrastructural parameters.

We took advantage of the Kullback–Leibler Divergence (DKL) as a measure for information loss (measured in bits) when modelling one probability distribution (i.e., human acutely demyelinated CNS tissue axons) with another, simpler or more easily attainable data probability distribution (i.e., data from *MiniSWINE*). We next compared the DKL when modelling the distributions of axonal thickness and g-ratio of the human de- and, respectively, remyelinated tissue, as well as the distributions of axonal thickness and g-ratio of *aLPC/aCTRL* and *sLPC/sCTRL* minipig tissue. In the acute stage, regarding axonal thickness, the intrinsic discrepancy of approximating the *aHum*

distribution was lower when using *aLPC* (DKL_aLPC = 0.0087 bits) than when using *aCTRL* tissue (DKL_aCTRL = 0.114 bits). Regarding the g-ratio, the intrinsic discrepancy was also lower when using *aLPC* (DKL_aLPC = 0.0003 bits) than when using *aCTRL* (DKL_aCTRL = 0.019 bits). In the subacute stage, the intrinsic discrepancy regarding the axonal thickness when modelling *sHum* with *sLPC* (DKL_sLPC = 0.0004 bits) was also lower than when employing *sCTRL* (DKL_sCTRL = 0.043 bits). The g-ratio could also be approximated with less information loss when using *sLPC* (DKL_sLPC = 0.0007 bits) than via *sCTRL* (DKL_sCTRL = 0.0082 bits). The DKL analysis showed that the LPC groups' ultrastructural features modelled human features of cerebral demyelination.

Discussion

We aimed in this study to demonstrate the feasibility of validly simulating acute demyelination followed by at least remyelination in a large animal model, reflecting what is known to occur in human inflammatory disorders of the CNS and allowing follow-up and characterisation using MR-, PET-imaging and microscopy.

We chose minipigs to study de- and remyelination (1) because they have relatively large gyrencephalic brains, (2) a high degree of neuroanatomical similarity to humans, including a similar white-to-grey matter (WM:GM) ratio (∼60:40), as well as (3) a manageable adult mass of around 60 kg.[9,49] The latter aspect is relevant to stereotaxy compared to fattening pigs since navigational coordinates for stereotaxy can shift during brain and body growth. This fact restricts longitudinal precision neuroanatomy studies to adult animals, which, for fattening pigs, due to their size and body mass, would pose significant infrastructural problems in using diagnostic devices analogous to human clinical use. Finally, minipigs are easily maintained in controlled conditions.[9]

For this, we induced reversible, spatially and temporally controlled demyelination using precise, stereotactic delivery of LPC via CED. To this end, we chose to develop an EMTS and a surgical-imaging-microscopy platform, *MiniSWINE*, which, due to its modular construction, is compatible with adaptations, e.g., to implement translational developments. One of the

Iba1 (microglia), NeuN (neuronal somata), CD3 (lymphocytes), CD68 (monocytes/macrophages). d) From left to right: areas of LFB signal loss (i.e., demyelination), Olig2+ cell densities per $300 \times 300\ \mu m^2$ ROI, proportion of area containing activated GFAP+ astrocytes in $1 \times 1\ mm^2$ ROI, proportion of area containing reactive Iba1+ microglia in $1 \times 1\ mm^2$ ROI, NeuN+ cell densities per $300 \times 300\ \mu m^2$ ROI, CD3+ cell densities per $300 \times 300\ \mu m^2$ ROI. We refrained from CD68 quantification because of a meagre signal-to-noise ratio, presumably due to low cross-species primary antibody affinity. Statistical tests were performed using the Kruskal–Wallis-Test, followed by Dunn's multiple comparisons test. n = 4, *$0.01 \leq p \leq 0.05$, **$0.01 \leq p \leq 0.001$, ***$p \leq 0.001$.
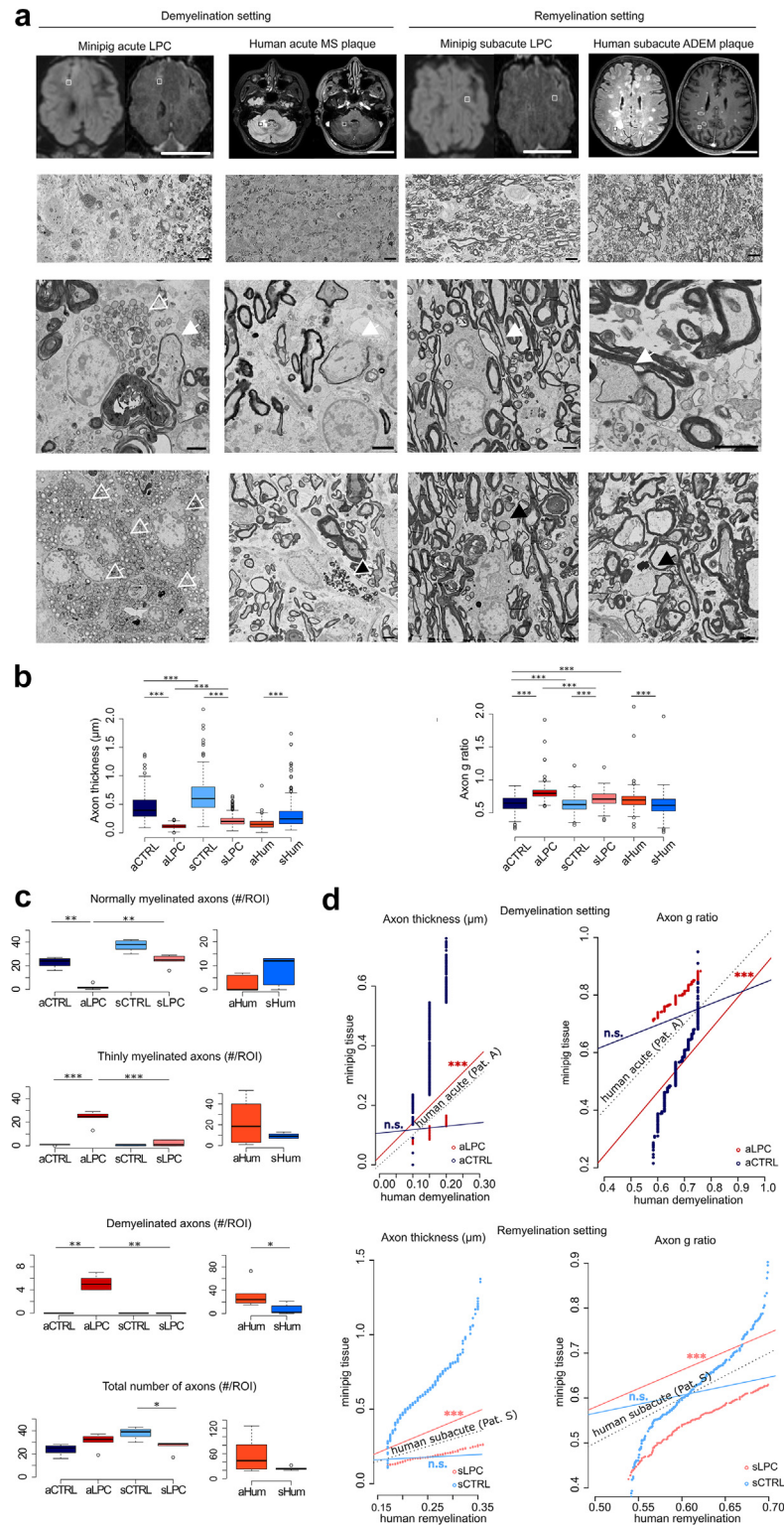
Fig. 6: Comparison of *MiniSWINE* and human demyelinating CNS disease biopsy ultrastructure. a) 1st row: Pairwise T2FLAIR and T1Gd axial MRI slices illustrating, in the case of the minipigs (from the left, columns 1 and 3), the areas where the autopsy was performed and, in the case of the humans (from the left, columns 2 and 4), the areas where biopsies were performed. White/black bounding boxes indicate approximate

initial challenges was to design a cannula that achieved an optimal, spherical substance spread function at canonical CED injection rates, which would also be compatible with readily available single-use catheters. In contrast to previously reported OTS, the EMTS we developed for this application was not limited by catheter, sensor wire or cannula bending in the tissue since the tracking targeted the instrument's tip and not the instrument shaft's initial part. Also, as EMTS does not require visual access for a camera, handling the navigated drill guide by the operator on challengingly small surfaces such as the forehead is more accessible than in the case of OTS by preventing line-of-sight issues faced by contemporary neurosurgical navigation systems.

However, a notable limitation of the *MiniSWINE* EMTS was interference with metals near the surgical field, which could not be eliminated. Indeed, in one of forty instances, we were confronted with the magnetisation of the cannula, which required its replacement during surgery, an issue not occurring in OTS. This issue could be compensated for practical purposes by ensuring appropriate spacing between the EMTS and metallic surgical instruments, providing satisfactory injection precision. Nevertheless, the fact that salient anatomical points *in vivo*, as opposed to *in vitro*, are registered on the skin, which can physiologically shift within certain limits in relation to subcutaneous tissue, contributed to the discrepancy between the navigation precision *in vitro* (0.23 ± 0.03 mm) vs. *in vivo* (1.54 ± 0.4 mm).

Two main factors conditioned the variability of the target injection coordinates. Firstly, in contrast to rodent brain LPC injections, where invariable stereotactic coordinates relative to an anatomical structure (e.g., bregma) can be formulated and translated between individuals,[50] in minipigs, due to the larger brain volume (approximately 70–80,000 mm^3 in our cohort), this approximation does not hold. In our experience with the minipig brain, avoiding vasculature of more than 0.8 mm diameter is necessary, exhibiting specific anatomical interindividual variability throughout the injection trajectory. Secondly, since the minipig brain is several orders of magnitude larger than, for instance, mouse brains (volumes of 400–500 mm^3),[50] a "one-size-fits-all" approach can have unwanted consequences.

A critical consideration once having established the platform *MiniSWINE* from the technical standpoint, was validating it against the MAGNIMS consortium MRI sequences performed on the same devices in a clinical setting as would be the case for the diagnosis and follow-up of a chronic inflammatory demyelinating disorder in human patients, such as for MS. Inter-correlating, reproducibly higher T2FLAIR, T1Gd and DIR signal susceptibilities in the treatment, but not in the control group, indicated a tissue-effect, compatible with demyelination, as well as a partial permeability increase of the blood-brain barrier (Gd uptake) triggered at the acute stage by the intraparenchymal LPC injection. The absence of correlations between SWI and the sequences above in the treatment and the control group suggested that the inherent microhaemorrhage along the injection trajectory did not significantly confound LPC-induced effects. One aspect of SWI-related MRI sequences, which we did not investigate in light of the known accumulation of iron in macrophages in active lesions and shadow plaques,[47] would be potential sensitivity to ongoing inflammation or even, in the case of quantitative susceptibility imaging (QSM), sensitivity to myelin content, which could be exploited as a biomarker for remyelinated lesions.[51] Results from our longitudinal MRI follow-up alone were, in principle, compatible with subsequent remyelination. Still, since none of the current MAGNIMS consensus sequences can reliably track remyelination,[2] we needed additional, more specific imaging and parallel histopathological characterisation of lesion evolution to validate our hypothesis. As a proof-of-concept for testing minimally invasive, novel imaging biomarkers that could help tackle the current challenge of detecting incipient remyelination, we resorted to *in vivo* [^{11}C]-PIB-PET imaging, with the aid of which we could demonstrate a correlation between subsiding T2FLAIR and T1Gd signals and restoration of PIB-uptake, as a potential starting point for evaluating this technique in future (human) studies. We also showed via parallel investigation *in vivo* by MRI and *ex vivo* by histopathology that we could follow-up signals of demyelination for weeks without confounding due to potential intercurrent mechanical tissue damage or perilesional intracerebral haemorrhage.

---

areas from which a small sample was analysed with SEM (see also Methods). 2nd row: SEM-micrographs from *aLPC*, *aHum*, *sLPC*, *sCTRL* and, respectively, *sHum* groups, scale bar = 10 μm. 3rd row, 4th row: High magnification SEM-micrographs, scale bar = 2 μm. White arrows = thin myelin; hollow white arrows = lipid droplets in foam cells; black arrows with white outline: astrocytic lipid droplets and lysosomal inclusions; black arrows: axonal pathology. b) Quantification of axonal and myelin pathology of axonal diameter (above), as well as g-ratio (below) in all study groups, including *aHum* and *sHum*. c) Quantification of myelin pathology. Numbers of, from the left, normally myelinated, thinly myelinated and demyelinated axons per 10 × 10 μm ROI. b and c) Kruskal–Wallis test followed by Dunn's multiple comparisons test, *$0.01 \leq p \leq 0.05$, **$0.01 \leq p \leq 0.001$, ***$p \leq 0.001$. d) Comparisons of the predictive power of linear regression models of axonal thickness and g-ratio from *MiniSWINE* (the linear model itself as a straight line) compared to the human linearised data, represented by the dotted straight line. The nearer the trajectory of the coloured line was to one of the dotted lines, the better the prediction of *MiniSWINE* relative to human data was. Statistical significance and *p* values were determined by likelihood ratio tests, ***$p \leq 0.001$, n.s. = not significant.

The de-/remyelination dynamics observed in *Mini-SWINE* differed somewhat from those described in rodent -models.[18,52] The latency to remyelination took between 20 dpi (intermediate stage) and 30 dpi (subacute stage). It resembled the 2–3 weeks described in rodent studies[18,53] more than the incomplete remyelination, even six weeks post-induction, in other large animal models.[16,17] These findings indicate that in contrast to rodents, where remyelination is largely completed around 14–21 dpi,[18,53] in the minipig, even at 30 dpi in the subacute stage, there is coexistence between a subsiding but still active demyelinating component and tissue restorative mechanisms. This observation aligns with recent reports describing the lesion volume and species-inherent differences in OPC infiltration of the lesion, proliferation and differentiation as the main factors determining the remyelination status.[17] We cannot exclude age-dependent effects on the latency of the remyelination,[16] but consider this unlikely due to the homogenous cohort of young adult minipigs used (aged 19 ± 1 months, assuming a life expectancy of 15–20 years). Future work with increased imaging density and specific labelling of OPCs may help further clarify the interspecies differences.

We then demonstrated experimentally that ultrastructural indicators of de- and remyelination from *MiniSWINE* matched human biopsy data from two patients in distinct phases of a demyelinating CNS inflammatory process by exhibiting similar lesion characteristics. The variation of axonal diameter across stages in the minipig brain was consistent with reports in patients with acute and subacute MS lesions.[48] Nevertheless, we had to compare WM axonal diameters and g-ratios from different human brain regions (*aHum* was a biopsy from the cerebellar WM, while *sHum* was from the subcortical WM), which restricted the comparability of results between the demyelinating and remyelinating human conditions. We observed homogenous de- and remyelination patterns irrespective of the injection location within the centrum semiovale, even though existing reports in the literature hint towards subtle interregional differences within different areas of the corpus callosum in rodent cuprizone models.[50,53] Interestingly, we found a certain degree of putatively secondary axonal pathology (around 15% of axons) inherent to the subacute treatment group, which deviates from the paradigm of a pure demyelinating non-inflammatory LPC-induced lesion in rodent studies and more closely resembles results from rabbit and macaque studies.[16,17] A previous study focused solely on the acute stage[15] but did not describe the pig brain's subacute LPC-induced and demyelinating lesion dynamics. Another result of our imaging data is that canonical MRI sequences may be indicative of, but tend to overestimate the extent of de-/remyelination, an implication also suggested in an EAE study in marmosets, where, however, due to purely immunohistochemical and not electron microscopic correlation, a layer of caution regarding lesion classification remains.[54]

One potentially critical aspect here is that in the remyelination setting, the proportion of axons with thin myelin, typical for remyelinated axons, is relatively low (on the order or 2%), which is counterintuitive, given that the lesions are still detectable by [^{11}C]-PIB-PET-MRI. However, MRI sequences stipulated by the MAGNIMS consortium do not specifically identify de- or remyelination events. Also, the [^{11}C]-PIB uptake correlates with myelination so that in a remyelinating lesion, one expects a lower contrast between the potential lesion and surrounding parenchyma, further lowering detectability. Therefore, astrogliosis, microglial and immune cell infiltration can also confound the imaging, especially in the case of the MRI, leading to an overestimation of the de-/remyelinated lesion core, which can, in our paradigm, be precisely determined on histological and ultrastructural basis. Also, since the LPC primarily induces demyelination with reactive inflammation, the translation of conclusions drawn from our model to demyelinating diseases such as MS, in which primary inflammation leads to demyelination, is limited.

On the whole, another limitation of the study was given by the low experimental numbers concomitantly examined with multimodal diagnostic methods, especially in the subacute group. On the one hand, this aspect was due to longitudinal imaging being performed in a single animal, leading to more lesions being generated in the acute stage than subacute lesions could emerge. On the other hand, we were constrained by local ethical regulations to establish the pipeline sequentially and simultaneously generate final data. Understandable ethical considerations also meant that lesions had to be asymptomatic, diverging from the situation in human demyelinating diseases such as MS.

To conclude, despite limitations, we established controlled cerebral de- and remyelination in a large animal model and validated it in a multimodal imaging and microscopy setting against existing and emerging biomarkers. We observed slower de- and remyelination than reported in homologous rodent models and, in parallel, a degree of secondary axonal pathology. This aspect may eventually depict corresponding processes occurring in human diseases better than rodent models. In this sense, *MiniSWINE* opens the avenue for immediate clinical translation to diagnostic procedures and new imaging biomarkers while representing a gateway to future testing of novel remyelinating agents. Furthermore, our proposed EMTS may enhance stereotactic substance delivery in human neurosurgery.

Appendix A. Supplementary data

Supplementary data related to this article can be found at https://doi.org/10.1016/j.ebiom.2024.104982.

References

1 Dendrou CA, Fugger L, Friese MA. Immunopathology of multiple sclerosis. *Nat Rev Immunol*. 2015;15:545–558.
2 Filippi M, Brück W, Chard DT, et al. Association between pathological and MRI findings in multiple sclerosis. *Lancet Neurol*. 2019;18:198–210.
3 Plemel JR, Liu W-Q, Yong VW. Remyelination therapies: a new direction and challenge in multiple sclerosis. *Nat Rev Drug Discov*. 2017;16:617–634.
4 Walhovd KB, Johansen-Berg H, Káradóttir RT. Unraveling the secrets of white matter@ bridging the gap between cellular, animal and human imaging studies. *Neuroscience*. 2014;276:2–13.
5 Ransohoff RM. Animal models of multiple sclerosis: the good, the bad and the bottom line. *Nat Neurosci*. 2012;15:1074–1077.
6 Procaccini C, De Rosa V, Pucino V, Formisano L, Matarese G. Animal models of multiple sclerosis. *Eur J Pharmacol*. 2015;759:182–191.
7 Dolgin E. Minipig, minipig, let me in. *Nat Med*. 2010;16(12):1349.
8 Fischer K, Schnieke A. Extensively edited pigs. *Nat Biomed Eng*. 2021;5(2):128–129.
9 Ardan T, Baxa M, Levinská B, et al. Transgenic minipig model of Huntington's disease exhibiting gradually progressing neurodegeneration. *Dis Models Mech*. 2019;13:dmm041319.
10 Flisikowska T, Egli J, Flisikowski K, et al. A humanized minipig model for the toxicological testing of therapeutic recombinant antibodies. *Nat Biomed Eng*. 2022;6:1248–1256.
11 Wakeman DR, Crain AM, Snyder EY. Large animal models are critical for rationally advancing regenerative therapies. *Regen Med*. 2006;1(4):405–413.
12 Hou N, Du X, Wu S. Advances in pig models of human diseases. *Anim Model Exp Med*. 2022;5(2):141–152.
13 Singer BA, Tresser NJ, Frank JA, McFarland HF, Biddison WE. Induction of experimental allergic encephalomyelitis in the NIH minipig. *J Neuroimmunol*. 2000;105(1):7–19.
14 Blakemore WF, Franklin RJM. Remyelination in experimental models of toxin-induced demyelination. *Curr Top Microbiol Immunol*. 2008;318:193–212.
15 Kalkowski L, Malysz-Cymborska I, Golubczyk D, et al. MRI-guided intracerebral convection-enhanced injection of gliotoxins to induce focal demyelination in swine. *PLoS One*. 2018;13:e0204650.
16 Cooper JJM, Polanco JJ, Saraswat D, et al. Chronic demyelination of rabbit lesions is attributable to failed oligodendrocyte progenitor cell repopulation. *Glia*. 2023;71(4):1018–1035.
17 Sarrazin N, Chavret-Reculon E, Bachelin C, et al. Failed remyelination of the nonhuman primate optic nerve leads to axon degeneration, retinal damages, and visual dysfunction. *Proc Natl Acad Sci U S A*. 2022;119(10):e2115973119.
18 Cantuti-Castelvetri L, Fitzner D, Bosch-Queralt M, et al. Defective cholesterol clearance limits remyelination in the aged central nervous system. *Science*. 2018;359:684–688.
19 Mozafari S, Deboux C, Laterza C, et al. Beneficial contribution of induced pluripotent stem cell-progeny to Connexin 47 dynamics during demyelination-remyelination. *Glia*. 2021;69(5):1094–1109.
20 Hall SM. The effect of injections of lysophosphatidyl choline into white matter of the adult mouse spinal cord. *J Cell Sci*. 1972;10(2):535–546.
21 Denic A, Johnson AJ, Bieber AJ, Warrington AE, Rodriguez M, Pirko I. The relevance of animal models in multiple sclerosis research. *Pathophysiology*. 2011;18(1):21–29.
22 Mezydlo A, Treiber N, Ullrich Gavilanes EM, et al. Remyelination by surviving oligodendrocytes is inefficient in the inflamed mammalian cortex. *Neuron*. 2023;111(11):1748–1759.e8.
23 Koivukangas T, Katisko JPA, Koivukangas JP. Technical accuracy of optical and the electromagnetic tracking systems. *SpringerPlus*. 2013;2:90.
24 Pawlowsky K, Ernst L, Steitz J, et al. The Aachen Minipig: phenotype, genotype, hematological and biochemical characterization, and comparison to the Göttingen minipig. *Eur Surg Res*. 2017;58(5–6):193–203.
25 Bobo RH, Laske DW, Akbasak A, Morrison PF, Dedrick RL, Oldfield EH. Convection-enhanced delivery of macromolecules in the brain. *Proc Natl Acad Sci U S A*. 1994;91(6):2076–2080.
26 Sillay KA, McClatchy SG, Shepherd BA, Venable GT, Fuehrer TS. Image-guided convection-enhanced delivery into agarose gel models of the brain. *J Vis Exp*. 2014;87:51466. https://doi.org/10.3791/51466.

27 Wattjes MP, Ciccarelli O, Reich DS, et al. 2021 MAGNIMs CMSC NAIMS consensus recommendations on the use of MRI in patients with multiple sclerosis. *Lancet Neurol*. 2021;20:653–670.

28 Thompson AJ, Banwell BL, Barkhof F, et al. Diagnosis of multiple sclerosis: 2017 revisions of the McDonald criteria. *Lancet Neurol*. 2018;17:162–173.

29 Brant-Zawadzki MN, Gillan GD, Nitz WR. MP RAGE: a three-dimensional, T1-weighted, gradient-echo sequence–initial experience in the brain. *Radiology*. 1992;182(3):769–775.

30 Riche M, Marijon P, Amelot A, et al. Severity, timeline, and management of complications after stereotactic brain biopsy. *J Neurosurg*. 2022;136(3):867–876.

31 Stankoff B, Freeman L, Aigrot M-S, et al. Imaging central nervous system myelin by positron emission tomography in multiple sclerosis using [methylŒ 11C] R (T2 methylaminophenylI V hydroxybenzothiazole. *Ann Neurol*. 2011;69:673–680.

32 Mathis CA, Wang Y, Holt DP, Huang G-F, Debnath ML, Klunk WE. Synthesis and evaluation of 11C-labeled 6-substituted 2-arylbenzothiazoles as amyloid imaging agents. *J Med Chem*. 2003;46(13):2740–2754.

33 Lopresti BJ, Klunk WE, Mathis CA, et al. Simplified quantification of Pittsburgh Compound B amyloid imaging PET studies: a comparative analysis. *J Nucl Med*. 2005;46(12):1959–1972.

34 Zhanmu O, Yang X, Gong H, Li X. Paraffin-embedding for large volume bio-tissue. *Sci Rep*. 2020;10:12639.

35 Schindelin J, Arganda-Carreras I, Frise E, et al. Fiji: an open-source platform for biological-image analysis. *Nat Methods*. 2012;9(7):676–682.

36 Rosen GD, Harry JD. Brain volume estimation from serial section measurements: a comparison of methodologies. *J Neurosci Methods*. 1990;35(2):115–124.

37 Gundersen HJ, Jensen EB. The efficiency of systematic sampling in stereology and its prediction. *J Microsc*. 1987;147(Pt 3):229–263.

38 Kislinger G, Gnägi H, Kerschensteiner M, Simons M, Misgeld T, Schifferer M. ATUM-FIB microscopy for targeting and multiscale imaging of rare events in mouse cortex. *STAR Protoc*. 2020;1(3):100232.

39 Stikov N, Campbell JSW, Stroh T, et al. Quantitative analysis of the myelin g-ratio from electron microscopy images of the macaque corpus callosum. *Data Brief*. 2015;4:368–373.

40 de Paula Faria D, de Vries EFJ, Sijbesma JWA, Buchpiguel CA, Dierckx RA, Copray S. PET imaging of glucose metabolism, neuroinflammation and demyelination in the lysolecithin rat model for multiple sclerosis. *Mult Scler J*. 2014;20:1443–1452.

41 Holman C, Piper SK, Grittner U, et al. Where have all the rodents gone? The effects of attrition in experimental research on cancer and stroke. *PLoS Biol*. 2016;14:e1002331.

42 Pomfret RJ, Miranpuri GS, Sillay KA. The substitute brain and the potential of the gel model. *Ann Neurosci*. 2013;20:118–122.

43 Miranpuri GS, Hinchman A, Wang A, et al. Convection enhanced delivery: a comparison of infusion characteristics in ex vivo and in vivo non-human primate brain tissue. *Ann Neurosci*. 2013;20:108–114.

44 Mehta AM, Sonabend AM, Bruce JN. Convection-enhanced delivery. *Neurotherapeutics*. 2017;14:358–371.

45 Nelson F, Poonawalla AH, Hou P, Wolinsky JS, Narayana PA. 3D MPRAGE improves classification of cortical lesions in multiple sclerosis. *Mult Scler*. 2008;14:1214–1219.

46 Huitema MJD, Strijbis EM, Luchicchi A, et al. Myelin quantification in white matter pathology of progressive multiple sclerosis post-mortem brain samples: a new approach for quantifying remyelination. *Int J Mol Sci*. 2021;22:12634.

47 Popescu BF, Frischer JM, Webb SM, et al. Pathogenic implications of distinct patterns of iron and zinc in chronic MS lesions. *Acta Neuropathol*. 2017;134(1):45–64.

48 Albert M, Antel JP, Brück W, Stadelmann C. Extensive cortical remyelination in patients with chronic multiple sclerosis. *Brain Pathol*. 2007;17:129–138.

49 Vodicka P, Smetana K Jr, Dvoránková B, et al. The miniature pig as an animal model in biomedical research. *Ann N Y Acad Sci*. 2005;1049:161–171.

50 Steelman AJ, Thompson JP, Li J. Demyelination and remyelination in anatomically distinct regions of the corpus callosum following cuprizone intoxication. *Neurosci Res*. 2012;72(1):32–42.

51 Rahmanzadeh R, Galbusera R, Lu PJ, et al. A new advanced MRI biomarker for remyelinated lesions in multiple sclerosis. *Ann Neurol*. 2022;92(3):486–502.

52 Cunha MI, Su M, Cantuti-Castelvetri L, et al. Pro-inflammatory activation following demyelination is required for myelin clearance and oligodendrogenesis. *J Exp Med*. 2020;217:e20191390.

53 Werkman IL, Lentferink DH, Baron W. Macroglial diversity: white and grey areas and relevance to remyelination. *Cell Mol Life Sci*. 2021;78(1):143–171.

54 Donadieu M, Lee NJ, Gaitán MI, et al. In vivo MRI is sensitive to remyelination in a nonhuman primate model of multiple sclerosis. *Elife*. 2023;12:e73786.